
3-D AUTOMATIC ANATOMY-BASED IMAGE REGISTRATION IN PORTAL IMAGING

by

Luc M. Sirois
Medical Physics Unit
McGill University, Montreal
January 1999

A thesis submitted to the Faculty of Graduate
Studies and Research in partial fulfillment of
the requirements of Master of Science

0-612-50880-3

ABSTRACT

A three dimensional, automatic, anatomy-based system for portal verification has been developed based on an FFT implementation of Pearson's correlation coefficient (PCC). The PCC requires no anatomy or point-pair identification, is robust when encountering changes in scaling and shifts in image amplitudes and requires no priori knowledge of the anatomy, which makes it an ideal candidate for portal-to-DRR image registration. Features for matching are selected from orthogonal portal images and compared to the corresponding megavoltage DRR. The position of the highest correlation value is then converted into beam-to-patient geometry and compared with the actual patient setup. By continuously generating DRRs, the system is capable of verifying translation errors, in-plane rotation and out-of-plane rotation errors. The mean accuracy of translation and rotation registrations tests were 0.58 mm and 0.79° respectively for DRR-to-DRR matching, and 1.22 mm and 1.31° respectively for portal-to-DRR matching.

RÉSUMÉ

Une méthode automatique, tri-dimensionnelle, basée sur la position relative de traits anatomiques, pour la vérification du positionement à l'aide d'images portales a été developée. Le coéfficient de correlation Pearson (PCC) a été utilisé comme engin de correlation, car ce dernier ne requiert pas d'identification anatomique, est indépendant des déplacements et des changements d'amplitudes de l'intensité des images, et n'exige aucune connaissance antérieure de l'anatomie. Ce tout rend le PCC un candidat idéal pour la comparaison des images portales avec des radiographies reconstruites digitalement (DRR). À partir de deux images portales orthogonales, un trait anatomique de chaque projection est selectionné et comparé au DRR megavoltage correspondant. La position du coéfficient de correlation maximum révèle les paramètres qui simulent la paire de DRR ressemblant le plus aux images portales orthogonales et permet d'identifier des erreurs dans le positionnement du patient. En générant continuellement de nouveaux DRRs, la méthode présentée est capable de vérifier les erreurs de translations et de rotations hors-plan et dans le plan de l'image. L'erreur moyenne obtenue pour dépister les erreurs de translations et de rotations est de 0.58 mm et 0.79° respectivement pour les essaies DRR-à-DRR et de 1.22 mm et 1.31° respectivement lors des essaies portale-à-DRR.

AKNOWLEDGMENTS

I would like thank my supervisor, Dr. B. G. Fallone, for the guidance and support he provided throughout the year. He proved to be a source of encouragement and insight needed to achieve the completion of my thesis. I am also grateful for the financial support he provided during the duration of this work.

I am also grateful to several staff and students at the McGill University Medical Physics Unit. In particular, Dr. E. B. Podgorsak, for sharing his knowledge and insight during the past two years. I greatly appreciate the valuable suggestions and discussions I had with Dr. D. H. Hristov during the last few months of this work. I would also like to acknowledge Mr. H. Patriocio for teaching me the detailed set-up and procedures involved in stereotactic radiosurgery at the Montreal General Hospital. I wish to thank fellow students Heather Thompson for her vivid discussions and moral support and François Deblois for sharing his computer programming knowledge.

Financial assistance for this work was gratefully provided by the Medical Research Council of Canada (grant number: MT-13118).

Finally, I cannot begin to thank my girlfriend, Faby Gagné, and my parents for their love and support throughout the years.

Table of Contents

CHAPTER 1

CHAPTER 2

CHAPTER 3

CHAPTER 4

CHAPTER 5

Chapter 1:

Introduction

1.1 PORTAL IMAGING

The aim of radiotherapy is to deliver a lethal dose to a treatment volume while minimizing the dose to the surrounding healthy tissue. In order for the treatment to be successful, the dose must be properly delivered to the treatment volume. To verify the accuracy of the dose delivery, a detector, positioned on the opposite side of the patient, is exposed to the treatment beam. The resulting image, similar to a diagnostic image, is referred to as a portal image. By examining portal images acquired prior to the treatment, errors in the radiation field positioning with respect to the patient can be detected. The simplest way to acquire a portal image is to position a port film behind the patient for a short period during the beginning of the treatment or during the complete treatment depending on the film speed. Portal imaging was first reported by Hare et al who had adopted film for supervoltage rotational therapy verification.[1] The portal image acquisition process is identical to that used in diagnostic radiology. During exposure, photons are scattered and attenuated as they traverse the patient's body, modifying the number of photons that hit the detector along any given ray path. At any point on the portal image, the pixel intensity is dependent of the photon density impinging on the detector. Patient thickness and poor radiographic techniques do limit the quality of the portal images. Since portal images are acquired at megavoltage energies, Compton scattering is the major factor for causing poor quality radiographic images. Portal images, do however, allow one to see the treatment field shape and size along with bony anatomical features. At megavoltage energies, the mass attenuation coefficient of bone and brain matter are almost identical because of Compton interactions, which explains why portal images usually display smaller differences in contrast between soft tissue and bone than what's observed in diagnostic images.

Film remains the most common detector for portal imaging. Various film cassettes have been developed in an attempt to improve the resulting image quality. These cassettes usually consist of a metal screen that provides build-up and converts the incoming photons to electrons, which increases the films sensitivity.

On-line electronic portal imaging devices (EPID) are commercially available. These devices detect incoming photons and translate the information to a computer. Since the images are digital, the image can easily be enhanced to provide an image with superior contrast than that obtained with film detectors. Fluoroscopy-based systems, solid state devices, and scanning liquid ionization chambers represent the different types of EPIDs currently available. Fluoroscopy-based systems are essentially composed of a phosphor detector bound to a metal plate, a mirror and a video camera. Most of the incident high-energy photons transfer energy to electrons in the plate, which in turn, transfer their energy to the phosphor detector. This transfer of energy results in the emission of photons, which are reflected by the mirror and detected by the video camera and sent to a computer or video monitor for viewing. Solid state EPID systems consist of a phosphor detector and metal plate pair coupled to a matrix of photodiode-field effect transistors. The light produced in the phosphor/metal plate creates electron-hole pairs in the photodiode. The photodiode then behaves like a capacitor. The stored charge is read from each photodiode and digitized to form an image. Scanning liquid ionization chambers are based on the principle of the ionization chamber, except the sensitive volume is filled with iso-octane liquid instead of air. Two series of parallel wires perpendicularly cross the plane forming an ionization matrix. The resulting currents produced in each wire are read sequentially in a raster fashion and the signals are processed and displayed by a computer.

1.2 ACCURACY IN RADIOTHERAPY

Over the years, several developments in external beam radiotherapy have aimed to reduce the treatment margin of healthy tissue around the tumor. Refinement in treatment techniques allow sparing of healthy tissue, thus reducing the risk of complications, and even allows an escalation of the tumor dose to increase the probability of eradication. As the radiation fields become more conform to the shape of the target volume, it becomes apparent that one could miss the target volume without the ability to verify the position prior to treatment, thus damaging healthy tissue and allowing the disease to progress. In radiotherapy, studies show that the standard deviation in treatment-to-treatment variation in patient set-up position is 3 mm when portal films acquired prior to each treatment are compared.[2] This deviation does not vary significantly for different treatment sites. However, when the brain is the treatment site, the average discrepancy between portal films and simulator films is 5 mm. Although, immobilization devices, such as stereotactic frames, reduce treatment set-up positioning errors, a report on stereotactic radiosurgery reveals that the total uncertainty in treatment delivery and target localization is 2.4 mm.[3] However, this uncertainty quickly rises to 3.7 mm when a CT slice of 3 mm, instead of 2 mm slice, is employed. This is clearly unacceptable in radiosurgery where the accepted error in target volume determination is ± 1 mm and the accepted error in spatial accuracy in dose delivery is ± 1 mm.[4]

To obtain a certain level of accuracy in the treatment delivery and to avoid any discrepancies in positioning, position verification methods should be implemented in the treatment process. Portal films and EPIDs are still currently used to provide an easy and practical way of obtaining a view of the treatment beam boundaries and some anatomical landmarks. However, it becomes debatable whether a simple visual analysis of portal images is sufficient. Techniques were also developed to provide registration of treatment field boundaries in radiotherapy.[5,6] Although they provide efficient means to verify the consistency of the radiation field edges, they do not allow verification of the actual treatment set-up. Any positioning errors would not be detected. To provide an accurate method for treatment set-up verification, the optimal choice is a method for verifying the position anatomical features with respect to a reference coordinate system or with a reference image.

1.3 ANATOMY-BASED, TREATMENT SET-UP VERIFICATION METHODS

1.3.1 Two-dimensional (2-D), anatomy-based, position verification methods

A number of groups have investigated, anatomy-based, position verification methods based on the comparison of two 2-D images. Bijhold developed a method for determining set-up errors during radiotherapy by aligning features in simulator and portal images.[7] Patient placement deviations are quantified as a three-dimensional translation and, in-plane and out-of-plane rotations of the patient from the intended position and orientation. Portal and simulator images are digitized and manually converted to digital line graphs of the relevant features, such as field edges, bony structures, match points and markers. Using a mouse-driven interface, the user can interactively align the digital line graph images and quantify any patient set-up errors. However, the technique produces erroneous results for of out-of-plane rotations larger than 2° or translations larger than 1 cm and is incapable of determining the rotation axis of an out-of-plane rotation, i.e. gantry or couch rotation. Since the alignment is interactive and the line graphs are manually created, inter-observer variability is non-negligible. Also, because portal and simulator images do not give complete information about the three-dimensional position of anatomical structures in the patient, comparing these images can only yield limited information.

Balter et al developed a method for patient position verification in radiotherapy capable of determining differences between projection radiographs.[8] A user interface allows identification of points or curves seen on both images. The algorithm matches one or more sets of corresponding open curves and point pairs to determine a global geometric transformation between the radiographs. This technique, however, cannot assess out-of-plane rotations of the patient. In addition, it is difficult to select the same starting and ending points on corresponding curve segments from two different images.

Gilhuijs and van Herk developed a method for automatic inspection of patient set-up from portal image pairs.[9] The method utilizes chamfer matching[10] as the matching algorithm and it essentially performs pattern recognition during matching. From the portal image, extraction images are created by automatically enhancing anatomical structures using an edge–extraction filter. The reference image is created after the user has directly drawn anatomical features into the simulator image. A cost function assesses the goodness of the fit between the extraction image and the reference image. When the cost is minimal, it generally implies that the drawing is aligned with its corresponding feature in the image. Once again, this method requires delineation of bony details and outlining the reference anatomy. The performance of the anatomy matching is heavily dependent of the quality of the anatomy extraction and, in some cases, some bone edges do not appear.

Moseley and Munro developed a semi-automated method for registering anatomical features on corresponding pairs of portal images using a cross-correlation approach.[11] The registration process is divided into two steps. During the first step, the cross-correlation operator registers user-selected anatomical features obtained from both corresponding portal images. During the second step, the technique registers the portal image pair by using the centre of the correlated regions as match points. Although the technique proved to produce accurate results and utilizes two different imaging planes for image registration, it is still limited by the 2-D nature of the portal images, thus it is only capable of detecting translations and in-plane rotations of the patient.

Hristov and Fallone developed a method for registering anatomical features on portal images and corresponding digitally reconstructed radiographs (DRR) using an Fast-Fourier Transform (FFT) implementation of Pearson's correlation coefficient.[12] The DRR, discussed in detail in Sec. 3.1.1.3 of Chapter 3, is meant to simulate a conventional radiograph using the three-dimensional CT data. It is obtained when a CT-volume, which can be visualized as a block of cubic voxels, is transformed into a 2-D image using ray tracing, thus mimicking a regular radiograph. A region of interest, containing anatomical features, is selected from a DRR reference image and registered with a portal test image that might contain in-plane rotations or translations. The algorithm proved to be more robust for image registration when compared with similar techniques based on the normalized correlation coefficient[13] since it is invariant under differences in scaling and shifts in pixel intensities. However, the method was only implemented for 2-D registration and the algorithm was not tested for detecting out-of-plane rotations.

The two-dimensional verification of position provide relatively accurate results under controlled situations. However, quantification of patient rotations in planes other than the imaging plane (out-of-plane rotations) is difficult. Because portal and simulator images do not give complete information about the three-dimensional position of anatomical structures in the patient, the comparison of portal to simulator images can only yield limited information. In addition, with 2-D position verification techniques, an out-of-plane rotation can be interpreted as a translation, resulting in erroneous registration.[7,14] The accurate determination of patient set-up in three dimensions could also allow a better estimation of the dose.[15]

1.3.2 Three-dimensional (3-D), anatomy-based, position verification methods

The limitations imposed by many of the 2-D position verification methods led to developments of new techniques capable of 3-D position verification techniques. The need to determine out-of-plane rotations led to the development of 3-D position verification methods that involve registration of portal or simulator images with DRRs. Lemieux et al developed an automatic, image correlation-based, method to verify the patient's position prior to radiosurgery using orthogonal diagnostic radiographs and

DRRs.[16] DRRs are generated for various projection parameters and iteratively compared with two diagnostic radiographs until the best match is found. Mean translation and rotation alignments are typically within 1 mm and 5° respectively. The system was however not used to match DRRs to portal images for "beam-on" verification.

Gilhuijs et al developed an automatic, three-dimensional, method for quantifying positioning errors using one set of CT data and two transmission images.[17] The technique uses chamfer matching for image registration and is basically a continuance of the 2-D method developed by Gilhuijs and van Herk.[9] This method extraction and enhancement of bony details of anatomy in the transmission images. In addition, the performance of the anatomy matching is heavily dependent of the quality of the anatomy extraction and the accuracy of the method decreases with smaller field sizes. The authors utilize a series of filters and edge enhancement tools, but provides no assurance that these tools are position independent and robust under different image acquisition conditions. In addition, the method's accuracy also decreases with smaller fields in the portal image.[11,17] The accuracy of the system is approximately 1 mm and 1° along each axis for translation and rotation axis

Murphy developed an image registration method for frameless radiosurgery based on chi-square statistic algorithm.[18] However, this method was developed for use with a Cyberknife and employs diagnostic level images and has not been used with portal images for "beam-on" verification.

Otto and Fallone developed an interactive 3-D method for position verification prior to stereotactic radiosurgery by comparing an orthogonal pair of portal images with corresponding DRRs.[19,22] An histogram-shift edge detection algorithm[20] is applied to the DRRs to delineate bony structures. Using a mouse driven interface, the DRR can be manipulated in either the anterior-posterior or lateral view to match with the portal image. As the user manipulates one DRR, the DRR in the orthogonal view is transformed accordingly. When the user judges that the DRRs in both views are correctly matched to the portal images, the DRR projection parameters are compared with the actual beam-to-patient geometry to reveal any positioning errors. Although this interactive method provides accurate results, inter-user variability is responsible for over 0.8 mm of the system error, which could be eliminated by automating the system. The reported mean radial error of this technique is 1.9 mm, but no rotation alignment analysis is offered.

Lujan et al recently developed a technique for two-dimensional portal to DRR registration.[21] Portal images, containing known rotation and translation errors, are acquired and prominent anatomical features are manually delineated. DRRs are then generated at different orientations from which anatomical features are manually delineated on each DRR. The portal contours are then compared to each contoured DRR using the open curve-matching algorithm developed by Balter et al.[4] The open curve matching algorithm determines the best matching delineated DRR by determining the minimum root-mean-square residual distance between points on user-defined curves. However, the technique requires the user to manually delineate each DRR contained in the DRR database. This task is very time consuming when considering that the method requires at least 50 delineated DRRs per view. Inter-user variability generates a certain degree of error in the final registration results. In addition, the method was only tested with images from one view only. An accuracy of 2° and about 1 mm for rotation and translation alignment was obtained in the anterior-posterior view, but one cannot conclude that it will be comparable in the lateral view.

1.4 THESIS OBJECTIVES

A technique for automatically verifying the location of the target with respect to the patient's anatomy in three dimensions is required to detect any positioning errors prior to radiotherapy. Many different 3-D approaches have been attempted and two main deficiencies appear:

- requires manual user delineation of anatomical feature,
- depends on the quality of the extraction of the anatomy.

The aim of this study was to develop a 3-D, image-correlation-based, method to automatically match digitally reconstructed radiographs (DRRs) to a pair of orthogonal portal images. It is a continuance of previous work done at our institution by Otto and Fallone,[19,22] who developed an interactive 3-D, anatomy-based, verification method for stereotactic radiosurgery and also incorporates work done at our institution on correlation-based matching by Hristov and Fallone.[12] The method verifies of the target position by matching a CT-volume to orthogonal pair of portal images acquired prior to the treatment. By using an FFT implementation of Pearson's correlation coefficient. Our method does not require user-delineation or automatic extraction of anatomical features and will not be hindered by varying field sizes.

The work detailed in this thesis aims to provide a description of our 3-D, anatomy-based, image registration method. In addition, a series of matching test results are presented to validate our method and to reveal its accuracy and performance for various anatomical features.

1.5 THESIS OUTLINE

Chapter 2 describes the engine of our image registration method, i.e. Pearson's correlation coefficient. This single element is the core of our automatic image registration method and dictates the level of attainable accuracy. An overview of the correlation and normalized correlation is first presented followed by the transformation of Pearson's correlation coefficient from the spatial to the frequency domain.

The experimental set-up and the overall registration procedure is discussed in Chapter 3. Each component of the procedure is then described in detail.

Chapter 4 provides an analysis of the accuracy of our system for determining translation, in-plane and out-of-plane rotation errors in DRR-to-DRR and Portal-to-DRR matching. Various anatomical features are used for matching and an analysis of each feature's accuracy for DRR-to-DRR matching is presented. Using the features best suited for DRR-to-DRR matching, results of portal-to-DRR image registration are presented to illustrate the accuracy and feasibility of our method in simulated clinical situations.

Finally, Chapter 5 summarizes our findings and presents our overall analysis of our method. A discussion of techniques for improving the accuracy of our current method is given with final remarks regarding our image registration technique.

1.6 REFERENCES

[1] H. F. Hare, J. Hale, and E. P. Pendergrass, "Physical and clinical aspects of supervoltage rotational therapy," Radiology 57, 157 (1951).

[2] I. Rabinowitz, J. Broomberg, M. Goitein, K. McCarthy, and J. Leong, "Accuracy of radiation field alignment in clinical practice," Int. J. Radiat. Oncol. Biol. Phys. 11, 1857-1867 (1985).

[3] M. C. Schell, F. J. Bova, D. A. Larson at al., "Stereotactic Radiosurgery, Report of Task Group 42 Radiation Therapy Committee," AAPM report no. 54, 6-7 (1995).

[4] E. B. Podgorsak, B. Pike, A. Olivier, M. Pla, and L. Souhami, "Radiosurgery with high energy photon beams: A comparison among techniques," Int. J. Radiat. Oncol. Biol. Phys. 16, 857-865 (1989).

[5] K. Eilersten, A. Skretting, and T. L. Tennvassas, "Methods for fully automated verification of patient set-up in external beam radiotherapy with polygon shaped fields," Phys. Med. Biol. 39, 993-1012 (1994).

[6] K. Leszczynski, S. Loose, and P. Dunscombe, "Segmented chamfer matching for the registration of field borders in radiotherapy images," Phys. Med. Biol. 40, 83-94 (1995).

[7] J. Bijhold, "Fast evaluation of patient set-up during radiotherapy by aligning features in portal and simulator images," Phys. Med. Biol. 36, 1665-1679 (1991).

[8] J. M. Balter, C. A. Pelizzari, and G. T. Y. Chen, "Correlation of projection radiographs in radiation therapy using open curve segments and points," Med. Phys. 19, 329-335 (1992).

[9] K. G. A. Gilhuijs and M. van Herk, "Automatic on-line inspection of patient setup in radiation therapy using digital portal images," Med. Phys. 20, 667-677 (1993).

[10] G. Bergefors, "Hierarchical chamfer matching: a parametric edge matching algorithm," IEEE Transactions on Pattern Analysis and Machine Intelligence 10, 849-865 (1988).

[11] J. Moseley and P. Munro, "A semiautomatic method for registration of portal images," Med. Phys. 21, 551-558 (1994).

[12] D. H. Hristov and B. G. Fallone, "A grey-level image alignment algorithm for registration of portal images and digitally reconstructed radiographs," Med. Phys. 23, 75-84 (1996).

[13] S. M. Jones and A. L. Boyer, "Investigation of an FFT-based correlation technique for verification of radiation setup," Med. Phys. 18, 1116-1125 (1991).

[14] J. Hanley, G. S. Mageras, J. Sun, and G. J. Kutcher, "The effects of out-of-plane rotations on two-dimensional portal image registration in conformal radiotherapy of the prostate," Int. J. Radiat. Oncol. Biol. Phys. 33, 1331-1343 (1995).

[15] J. Wong, E. D. Slessinger, R. E. Hermes, C. J. Offutt, T. Roy, and M. W. Vannier, "Portal dose images I: Quantitative treatment plan verification," Int. J. Radiat. Oncol. Biol. Phys. 18, 389-399 (1990).

[16] L. Lemieux, R. Jagoe, D. R. Fish, N. D. Kitchen, and D. G. T. Thomas, "A patient-to-computed tomography image registration method based on digitally reconstructed radiographs," Med. Phys. 21, 1749-1760 (1994).

[17] K. G. A. Gilhuijs, P. J. H. van de Ven, and M. van Herk, "Automatic three-dimensional inspection of patient setup in radiation therapy using portal images, simulator images, and computed tomography data," Med. Phys. 23, 389-399 (1996).

[18] M. J. Murphy, "An automatic six-degree-of-freedom image registration algorithm for image-guided frameless stereotaxic radiosurgery," Med. Phys. 24, 857-866 (1997).

[19] K. Otto and B. G. Fallone, "Frame slippage verification in stereotactic radiosurgery," Int. J. Radiat. Oncol. Biol. Phys. 41, 199-205 (1998).

[20] I. Crooks and B. G. Fallone, "A novel algorithm for the edge detection and edge enhancement of medical images," Med. Phys. 20, 993-998 (1993).

[21] A. Lujan, J. M. Balter, and R. K. en Haken, "Determination of rotations in three dimensions using two-dimensional portal image registration," Med. Phys. 25, 703-708 (1998).

[22] K. Otto, "3-Dimensional Anatomy-Based Verification in Stereotactic Radiosurgery," McGill University, M.Sc. dissertation (1997).

Chapter 2:

The Correlation Algorithm

2.1 INTRODUCTION

At McGill University, we have developed a technique for 3-D, anatomy-based, portal verification. Our method relies on the successful comparison of portal and megavoltage DRR images. To compare both portal and DRR images, it is necessary to perform a pixel-by-pixel comparison of two images of the same object. Such a comparison will reveal any relative translation shifts, rotational differences and even scale differences. The task of measuring the similarity between regions in two images is performed using a correlation technique. This chapter first presents basic correlation theory followed by a thorough description of the Pearson correlation coefficient, which we used. The engine of our technique, the FFT implementation of Pearson's correlation coefficient, is finally discussed along with particularities that are specific to our approach.

2.2 THE CORRELATION

The correlation technique consists of searching for regions in a search image where the image's grey-levels regionally coincide with the grey-levels of a search mask selected from a reference image. When measuring the similarity between regions in two images, it is important to obtain a measure of how well these image regions coincide. The search mask is compared with all possible locations throughout the search image and a measure of similarity is computed at each of these locations.

Let $f(x,y)$ be a search image of size $M \times N$ and $w(x,y)$ a search mask of size $J \times K$ selected from a reference image $g(x,y)$. It is possible to measure the degree of similarity between the search mask and the search image at a given location using

$$s(m,n) = \sum_x \sum_y (f(x,y) - w(x-m, y-n))^2, \qquad (2.1)$$

where $s(m,n)$ is the measure of similarity between the search mask and the search image, $m = 0, 1, 2, \ldots, M + J - 1$ and $n = 0, 1, 2, \ldots, N + K - 1$.[1] By expanding the right term in Eq. 2.1, we obtain

$$s(m,n) = \sum_x \sum_y f^2(x,y) - 2\sum_x \sum_y f(x,y)w(x-m,y-n) + \sum_x \sum_y w^2(x-m,y-n). \qquad (2.2)$$

From Eq. 2.2, it is clear that the intensities of *f(x,y)* and *w(x,y)* contribute individually to *s(m,n)* through the first and last term of the equation, i.e. $\sum_x \sum_y f^2(x,y)$ and $\sum_x \sum_y w^2(x-m,y-n)$ respectively. The last term remains constant for a given search mask throughout the matching process but, the first term varies continuously throughout the matching process as the search mask travels throughout the search image. However, it is the central term, i.e. $\sum_x \sum_y f(x,y)w(x-m,y-n)$, that is of interest. When the magnitude of the central term, which has a negative coefficient, is large, *s(m,n)* will be small. For this reason, whereas *s(m,n)* provides a good measure of mismatch, the central term provides a reasonable measure of match. This operation is referred to as the unnormalized correlation of *f* and *w* over the region described by *m* and *n*. The correlation can be written as

$$c(m,n)_{un} = [f \otimes w]_{m,n} = \sum_x \sum_y f(x,y)w(x-m,y-n), \qquad (2.3)$$

where *c(m,n)* is the correlation value at a given location *(m,n)*.[1]

From Eq. 2.3, it is possible to visualize that as *m* and *n* are varied, the search mask moves over the search image. At each location *(m,n)*, a correlation value is calculated. The maximum value of the correlation function identifies the position where the search mask best matches the search image.

Although Eq. 2.3 provides a measure of similarity between two images, it does not account for zero intensity values within the search mask or search image and depends strongly on the grey-level of the images. For example, if the search mask and search image contain a significant number of pixels with zero intensity, the correlation does not reveal the true best match. Normalizing the correlation would allow it to adjust to the characteristics of different images.

It is possible to normalize the correlation by dividing it by the maximum correlation value from the correlation of two exact image features. The normalized correlation will give values of up to unity, where the unity value represents a perfect match between a search mask and a search image. According to the Cauchy-Schwartz inequality,

$$c(m,n) \le \sqrt{\sum_x \sum_y f^2(x,y) \cdot \sum_x \sum_y w^2(x-m,y-n)} \,. \tag{2.4}$$

As Eq. 2.4 reveals, the equality holds only when $w(x,y) = C \times f(x,y)$, where C is a constant. Therefore, the right-hand term in Eq. 2.4 provides the maximum value of the correlation distribution. The normalized correlation coefficient can be written as

$$c_N(m,n) = \frac{\sum_x \sum_y f(x,y) w(x-m,y-n)}{\sqrt{\sum_x \sum_y f^2(x,y)} \cdot \sqrt{\sum_x \sum_y w^2(x-m,y-n)}}, \tag{2.5}$$

where $c_N(m,n)$ is the normalized correlation function for a given location (m,n), also referred to as the normalized cross-correlation.[2] The normalized cross-correlation can also be carried out in the frequency domain using the Fourier transform and the correlation theorem. An FFT based implementation of the normalized correlation coefficient increases the calculation speed significantly.[2,3]

2.3 PEARSON'S CORRELATION COEFFICIENT

Pearson's linear correlation coefficient is very similar to the normalized correlation in the sense that both are normalized to vary between -1 and 1, thus accounting for the differences in image grey-levels. In addition, Pearson's correlation coefficient accounts for changes in scaling and shifting in image intensities. Following the convention described by Hristov and Fallone,[4] it is generally defined as

$$r(m,n)=\frac{\sum_x\sum_y[f(x,y)-\bar{f}(x,y)]\cdot[w(x-m,y-n)-\bar{w}]}{\sqrt{\sum_x\sum_y[w(x-m,y-n)-\bar{w}]^2}\cdot\sqrt{\sum_x\sum_y[f(x,y)-\bar{f}(x,y)]^2}}, \quad (2.6)$$

where $m = 0, 1, 2,\ldots, M+J-1$, $n = 0, 1, 2,\ldots, N+K-1$, $\bar{f}(x,y)$ is the average value of the search window $f(x,y)$ in the region coinciding with the search mask $w(x,y)$ and $\bar{w}$ is the average intensity of the mask.[4] The summations are carried over the coordinates common to both the search mask and search window. By subtracting the average intensity of the search mask and the search image from their corresponding image intensities, Pearson's correlation becomes invariant under shifts, in addition to scale changes in image intensities.

As described by Hristov and Fallone,[4] a search mask $w(x,y)$ of size $J \times K$, containing anatomical features appropriate for matching, is selected from the reference image $g(x,y)$. As illustrated in Fig. 2.1, the search mask is then compared throughout the search window $f(x,y)$ of size $M \times N$ larger than $J \times K$, for every position (m,n) within the search window. A feature is judged appropriate for matching when it is sufficiently visible in both the reference image and search window. The search window is comprised of a test image that may have been translated and rotated with respect to the reference image. As the search mask is compared with the search window, a correlation value is calculated, which represents the closeness of the match between the two.

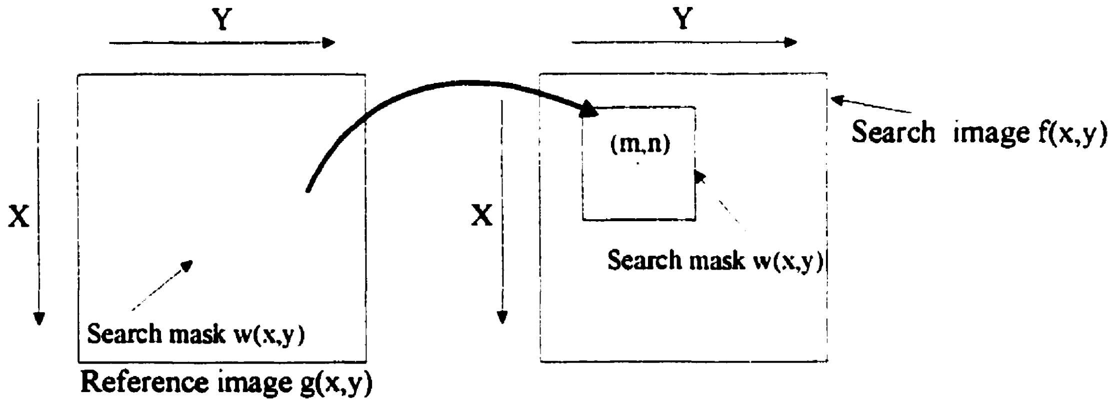

Figure 2.1: The search mask is compared for every position m and n within the search window. As the search mask sweeps through the search image, a correlation is calculated, representing the degree of similarity between the search mask at the search image at the position (m,n).

2.4 FFT IMPLEMENTATION OF PEARSON'S CORRELATION COEFFICIENT

Hristov and Fallone developed an FFT implementation of Pearson's correlation coefficient.[4] The FFT implementation can be derived using general correlation and Fourier transform theorems. The Fourier transforms of the search window $f(x,y)$ and the search mask $w(x,y)$ may be defined as $F(s,t) = \mathscr{F}[f(x,y)]$ and $W(s,t) = \mathscr{F}[w(x,y)]$ respectively, where $\mathscr{F}[\ ]$ is the Fourier transform. Using the correlation theorem,[5] the cross-correlation matrix may be written as

$$f \otimes w = f(x,y) \cdot w(x-m, y-n), \tag{2.7}$$

or as a function of the Fourier transforms of the functions, i.e.

$$f \otimes w = \mathscr{F}^{-1}[F(s,t) \cdot W^{*}(s,t)], \tag{2.8}$$

where $W^*(s,t)$ is the complex conjugate of $W(s,t)$ and $\mathscr{F}^{-1}[\ ]$ represents the inverse Fourier transform. It is possible to expand the numerator in Eq. 2.6 to obtain:

$$\sum_{x,y} f(x,y) \cdot w(x-m,y-n) - \sum_{x,y} f(x,y) \cdot \overline{w} - \sum_{x,y} \overline{f}(x,y) \cdot w(x-m,y-n) + \sum_{x,y} \overline{f}(x,y) \overline{w} \tag{2.9}$$

where terms 2 and 4 cancel each other. We finally obtain:

$$\sum_{x,y} f(x,y)\cdot w(x-m,y-n) - \sum_{x,y} \bar{f}(x,y)\cdot w(x-m,y-n)\,. \qquad (2.10)$$

The two terms in Eq. 2.10 lead to the following equalities:

$$\sum_{x,y} f(x,y)\cdot w(x-m,y-n) = \left[f \otimes w\right]_{m,n} \qquad (2.11)$$

and

$$-\sum_{x,y} f(x,y)\cdot \bar{w} = -\bar{w}(m,n)\left[\sum_{x,y} f(x,y)\right]_{m,n}\,. \qquad (2.12)$$

It is important to note that the subscript *(m, n)* indicates that the calculations are done pixel by pixel throughout the search window.

The search mask over the area common to the search mask and the search window can be defined as

$$\bar{w}(m,n) = \frac{1}{S(m,n)}\left[\sum_{x,y} w(x,y)\right]_{m,n}\,. \qquad (2.13)$$

where *S(m,n)* is defined as the area of the overlap and is given by

$$S(m,n) = [q \otimes p]_{m,n} = [\mathscr{F}^{-1}[Q(s,t) \cdot P^*(s,t)]]_{m,n}\ . \qquad (2.14)$$

where

$$p(x,y) = \begin{cases} 1, \text{if (x, y) is within the search mask} \\ 0, \text{otherwise} \end{cases} \qquad (2.15)$$

and

$$q(x,y) = 1, x = 1 \cdots M, y = 1 \cdots N, \qquad (2.16)$$

with their respective Fourier transforms

$$P(s,t) = \mathscr{F}[p(x,y)] \qquad (2.17)$$

and

$$Q(s,t) = \mathscr{F}[q(x,y)], \qquad (2.18)$$

where $P^*(s,t)$ is the complex conjugate of $P(s,t)$.

The sums over the common area of the search mask and the search window can be rewritten as

$$\left[\sum_{x,y} w(x,y)\right]_{m,n} = [q \otimes w]_{m,n} \text{ and} \tag{2.19}$$

$$\left[\sum_{x,y} f(x,y)\right]_{m,n} = [f \otimes p]_{m,n}. \tag{2.20}$$

The numerator of Eq. 2.6 can be rewritten as

$$\left[f \otimes w - \frac{(q \otimes w)(f \otimes w)}{q \otimes p}\right]_{m,n}. \tag{2.21}$$

The denominator of Eq. 2.6 can be analyzed in a similar manner. The first term of the denominator becomes

$$\sqrt{\sum_{x,y}\left[w(x-m,y-n)-\overline{w}\right]^2} = \sqrt{\sum_{x,y} w^2(x-m,y-n) - 2\overline{w}\sum_{x,y} w(x-m,y-n) + \sum_{x,y}\overline{w}^2(m,n)}$$

$$= \sqrt{\sum_{x,y} w^2(x-m,y-n) - S(m,n)\cdot\overline{w}^2(m,n)}$$

$$= \left[\sqrt{q \otimes w^2 - \frac{(q \otimes w)^2}{q \otimes p}}\right]_{m,n} \tag{2.22}$$

and similarly, the second term of the denominator becomes

$$\sqrt{\sum_{x,y}\left[f(x,y)-\bar{f}\right]^2}=\sqrt{\sum_{x,y}f^2(x,y)-2\bar{f}(m,n)\sum_{x,y}f(x,y)+\sum_{x,y}\bar{f}^2(m,n)}$$

$$=\left[\sqrt{f^2\otimes p-\frac{(f\otimes p)^2}{q\otimes p}}\right]_{m,n}. \qquad (2.23)$$

Using Eqs. 2.21, 2.22 and 2.23, Pearson's linear correlation coefficient can be rewritten in frequency space as

$$r(m,n)=\left[\frac{(f\otimes w)(q\otimes p)-(q\otimes w)(f\otimes p)}{\sqrt{(q\otimes w^2)(q\otimes p)-(q\otimes w)^2}\sqrt{(f^2\otimes p)(q\otimes p)-(f\otimes p)^2}}\right]_{m,n}. \qquad (2.24)$$

High correlation values will be obtained at the boundary regions of the search image. Therefore, the correlation *r(m,n)* has to be cropped accordingly to avoid detection of an erroneous maximum correlation value in the correlation distribution.

For situations where the search mask remains completely within the search image, Eq. 2.24 can be simplified by setting

$$q\otimes p=JK\hat{I}. \qquad (2.25)$$

$$q \otimes w^2 = \hat{I} \sum_{x=1}^{J} \sum_{y=1}^{K} w^2(x,y) \tag{2.26}$$

and

$$q \otimes w = \hat{I} \sum_{x=1}^{J} \sum_{y=1}^{K} w(x,y). \tag{2.27}$$

where $\hat{I}$ is a unitary matrix of size $[M - J + 1, N - K + 1]$. These substitutions will save computing time.

It is important to note that when using the FFT implementation of Pearson's correlation coefficient, the feature selected for matching is usually positioned near the centre of the search window. This is to maximize the probability of a successful match during registration. This also explains why the search window is not to be cropped at the same size as the search mask since after any displacement, the matching feature might not be fully included in the search window, resulting in a drop in the correlation at the correct location.

2.5 SUMMARY

Although other correlation algorithms, such as the normalized correlation coefficient,[2] are available for image registration, Pearson's correlation coefficient is more robust for our purposes. As Hristov and Fallone[4] describe, the normalized correlation coefficient is invariant under scaling of the image intensities [$g(x,y) \rightarrow C_1 \times g(x,y)$], but

Pearson's correlation coefficient is invariant under scaling and shifting of image intensities [$g(x,y) \rightarrow C_1 \times g(x,y) + C_2$], where C_1 and C_2 are constants. Pearson's correlation coefficient is more robust in cases where image might have undergone intensity changes due to variation in detector response or variations in dose delivery. from one treatment to another. Pearson's correlation coefficient is also very robust when encountering in-phantom scatter in portal images.[4]

Our technique does not require any anatomy delineation, edge enhancements or point pair matching in the search mask or search image. This eliminates most of the user error and inter-user variability encountered in many other anatomy-based, image registration methods detailed in Chapter 1. These features thus make Pearson's correlation coefficient well suited for automatic, anatomy-based, image registration.

2.6 REFERENCES

[1] R. J. Schalkoff, *Digital Image Processing and Computer Vision*, 1st ed. (Wiley, New York, 1989), pp. 279-284.

[2] S. M. Jones and A. L. Boyer, "Investigation of an FFT-based correlation technique for verification of radiation setup," Med. Phys. 18, 1116-1125 (1991).

[3] W. Pratt, *Digital Image Processing*, 1st ed. (Wiley, New York, 1978).

[4] D. H. Hristov and B. G. Fallone, "A grey-level image alignment algorithm for registration of portal images and digitally reconstructed radiographs," Med. Phys. 23, 75-84 (1996).

[5] R. N. Bracewell, *The Fourrier Transform and its Applications*, (McGraw-Hill, New York, 1978).

Chapter 3:

Materials and Methods

3.1 3-D AUTOMATIC, ANATOMY-BASED, IMAGE REGISTRATION

As previously discussed in Chapter 1, many anatomy-based position verification systems for radiotherapy have been developed. Several methods require anatomy identification, point pair matching, or some level of user interaction in the matching process. Other methods are not suited for 3-D registration because they cannot determine in-plane and/or out-of-plane rotations. At McGill University, we have developed an automatic, three-dimensional, method for image registration prior to the radiosurgical process. This work essentially combines the interactive, three-dimensional, anatomy-based, position verification technique developed by Otto and Fallone[1] with the image correlation algorithm developed by Hristov and Fallone.[2] The result is an automatic, 3-D, anatomy-based, position verification for radiosurgery. Numerous steps are involved for registering orthogonal pairs of portal images with corresponding DRRs reconstructed from CT-data. Figure 3.1 schematically illustrates our 3-D image registration method and shows the interactions between each component. This chapter discusses each component of the image registration process individually.

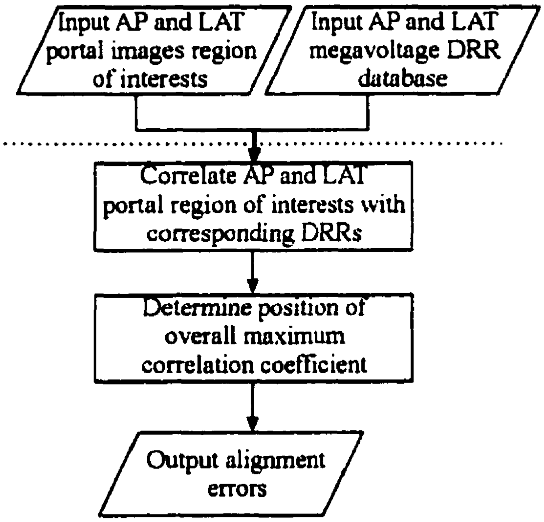

Figure 3.1: Schematic illustration of the various steps involved in our 3-D automatic image registration method.

3.1.1 Image acquisition and processing

The first step in our image registration method requires the input of an orthogonal pair of portal images (AP and LAT) and one CT-volume for a given patient or phantom.

3.1.1.1 Portal image acquisition

A diagnostic head phantom[3] is selected as our test object. A Leksell stereotactic frame[4], in combination with a portal localization box[5] affixed to the stereotactic frame, is fastened to the head phantom to confirm the exact position of the phantom in 3-D space. Using the etched grid on each face of the portal localizer box, the head phantom is positioned on the treatment table and aligned with the wall and ceiling lasers. Anterior-posterior (AP) and lateral (LAT) orthogonal portal image pairs of a diagnostic head phantom are acquired using a Clinac 18, 10 MV linac.[6] At least two 2D planar images are required to obtain a 3D localization of any point appearing in both images. The simplest approach is to acquire two orthogonal images of the region of interest. Using any arbitrary 3D coordinate system, the first planar image allows a preliminary 2D localization of the point of interest in the imaging plane. From the same coordinate system, the second image directly provides the third coordinate, which is located in the imaging plane, thus completing the 3D localization from the 2D images. For the linac used, the source-to-axis distance (SAD) is 100 cm. Kodak RP film in a Kodak X-Omatic L Radiation Therapy Cassette[7] are used as our detector. For each film, a first exposure of 5 monitor units is acquired with the surgical collimator in place and a field size of 4 × 4 cm^2. A second exposure of 2 monitor units is then made with the surgical collimator removed and an open beam exposing the entire head and frame attachment. From the projected image of the stereotactic frame and portal localization box assembly, the coordinates of the beam central axis is determined in stereotactic coordinates. Figure 3.2 illustrates our portal image acquisition set-up. The fiducial markers serve as a tool to determine the position of the beam isocentre relative to the stereotactic frame. The portal films are then digitized using a DuPont Lynx digitizer[8] at 844 × 1024 pixels with a pixel resolution of 0.43 mm. The digitized images are then cropped to 768 × 768 using the central beam axis image as the centre of our cropped image.

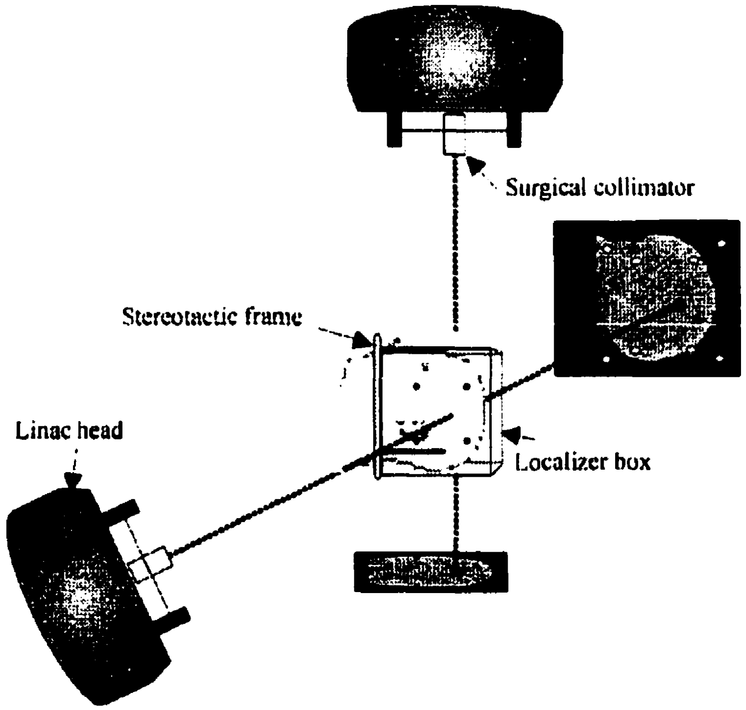

Figure 3.2: With the localizer box in place, the beam's central position may be determined in stereotactic coordinates using the fiducial markers appearing on each film. Two films are required to localize the beam in three-dimensions.

3.1.1.2 CT-data acquisition

As CT data set of the diagnostic head phantom, with the stereotactic frame and localization box assembly, is acquired with a Picker PQ-2000 CT-simulator at 130kV, with a 2 mm slice thickness and no gap between slices. The head phantom is positioned using the CT-lasers and the localization box. Each transverse slice comprises 512 × 512 pixels of 0.5469 mm in size. In order to maintain the correct image proportions, the CT-data is interpolated to 1 × 1 × 1 mm^3. To ensure that the image registration procedure is completely frame independent, the stereotactic frame image and fiducial markers are erased from the CT-data and does not appear on the AP and LAT DRRs.

3.1.1.3 Digitally Reconstructed Radiographs

The DRR is meant to simulate a conventional radiograph using the three-dimensional CT data. A DRR is obtained when a volume, which can be visualized as a block of cubic voxels, is transformed into a 2-D image using ray tracing, thus mimicking a regular radiograph. Goitein et al (1983) were among the first to use DRRs for use in radiotherapy.[9]

The ray tracing method is as follows. For each pixel in the output image, a ray is sent through the volume. Each voxel the ray passes through makes a contribution to the intensity of the pixel in the output image. A voxel's contribution depends on its opacity. This is defined as an additive light model because the rays accumulate voxel intensity contributions as they travel through the volume. For example, as illustrated in Fig. 3.3, a ray passing through a very opaque voxel will produce a DRR pixel with a higher intensity than the same ray passing through a translucent voxel.

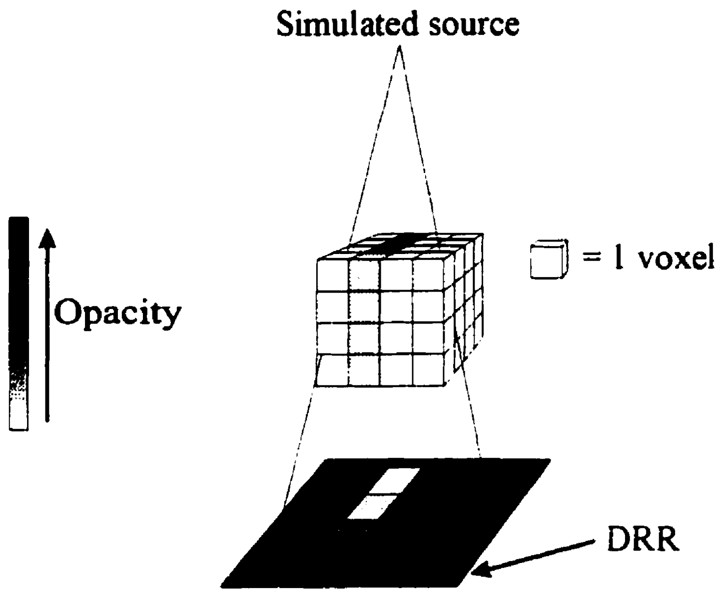

Figure 3.3. A CT data set can be visualized as an ensemble of individual voxels. The opacity of each voxel determines its intensity contribution to the DRR corresponding pixel.

When creating DRRs, one must ensure that the ray-tracing procedure is analogous to photons passing through matter and impinging on a detector. When a photon beam passes through matter, some photons are scattered or absorbed in the medium, but others will pass through and be detected at the detector, thus forming a radiographic image. As described by Johns and Cunningham, photon attenuation may be described by

$$I = I_o \cdot e^{-\mu \cdot x}, \tag{3.1}$$

where μ is the linear absorption coefficient of the medium, x is the thickness of the medium traversed by the photon beam, I and I_o are the final and initial photon intensities respectively.[10]

The previous expression can be rewritten for a slab of non-uniform material containing various linear attenuation coefficients:

$$I = I_o \cdot e^{(-\mu_1 \cdot \Delta x)} \cdot e^{(-\mu_2 \cdot \Delta x)} \cdot e^{(-\mu_3 \cdot \Delta x)} \dots \cdot e^{(-\mu_n \cdot \Delta x)}, \tag{3.2}$$

which can be simplified to become

$$I = I_o \cdot \sum_{i=1}^{n} \cdot e^{(-\mu_i \cdot \Delta x)}, \tag{3.3}$$

where μ_i is the attenuation coefficient of the medium at the i^th^ position along a given ray path and n is the number of arbitrary small ray paths of length Δx.

In the most general case, the previous expression is satisfactory to express the physical absorption of the photon beam, but one must not neglect the detector response when considering the image formation process. Detector response depends on the type of detector used and will greatly influence the resulting image. For film-based detectors, the optical density of the pixels on the final image can be expressed as

$$D = \Gamma \cdot \log\left(\frac{I}{I_o}\right), \tag{3.4}$$

where D is the optical density of the pixels in the image and Γ is a proportionality constant characteristic of the detector used.

Substituting Eq. 3.3 into Eq. 3.4 yields

$$D = -\Gamma \cdot \Delta x \cdot \sum_{i=1}^{n} \mu_i \tag{3.5}$$

and from this relation, it is possible to conclude that

$$D \propto \sum_{i=1}^{n} \mu_i \,, \tag{3.6}$$

which shows that the pixel intensity of the image is directly proportional to the sum of the linear attenuation coefficients through the ray path.

Voxels within a CT volume are individually represented by a CT number, in Houndsfield units (HU), which is related to the linear attenuation coefficient at that position in the volume in the following manner

$$CT\ number = K \cdot \frac{(\mu_m - \mu_{water})}{\mu_{water}}, \tag{3.7}$$

where K is a magnification factor equal to 1000 in most modern CT scanners, μ_{water} is the linear attenuation coefficient of water and μ_m is the linear attenuation coefficient of the given voxel. If we add the CT numbers along a ray path, the previous expression becomes

$$\sum_{i=1}^{n} CT\ number(i) = K \cdot \sum_{i=1}^{n} \frac{(\mu_m - \mu_{water})}{\mu_{water}}. \tag{3.8}$$

Manipulating Eq. 3.8, one can obtain

$$\sum_{i=1}^{n} CT\ number(i) = K \cdot \left(\frac{1}{\mu_{water}}\right) \cdot \sum_{i=1}^{n} \mu_i - K \cdot n, \tag{3.9}$$

which clearly shows the relation between the sum of the CT numbers and the linear attenuation coefficients along a ray path. One can conclude that

$$\sum_{i=1}^{n} CT\ number(i) \propto \sum_{i=1}^{n} \mu_i \tag{3.10}$$

and intuitively

$$D \propto \sum_{i=1}^{n} CT\ number(i). \tag{3.11}$$

The pixel intensity of the DRR is thus proportional to the sum of the CT numbers along the corresponding ray path. The brightness and contrast of a DRR can easily be modified to simulate various radiographic techniques.

To automatically match a DRR to a portal image successfully, it is preferable to have DRRs that simulate the contrast obtained in a typical portal radiograph. This can easily be done using lookup tables relating the CT number to the linear attenuation coefficient for the desired beam energy. Previous studies indicate that one can linearly relate the relative electron density ρ_e with the CT number for a given beam energy.[11]

The CT number for a given material will depend on the individual CT scanner used, the image reconstruction algorithm, the kVp used, the size of the field of view and the location of the material in the phantom.[12,13] For these reasons, it is important to verify the relationship between the electron density and the CT numbers for an individual scanner at a given beam energy.

Orfali determined the relationships linking the electron density to CT numbers for the Picker PQ-2000 CT-simulator used at the Montreal General Hospital by using a CT calibration phantom containing inserts of known compositions.[14] The CT numbers were measured directly from the CT scan of the calibration phantom and plotted against the corresponding electron densities ρ_e. The relationships are given by two equations:

$$\rho_e = 1.00090 + 0.00101 \cdot CT\ number \quad \text{(for CT numbers} \leq 100) \qquad (3.12)$$

$$\rho_e = 1.00080 + 0.00041 \cdot CT\ number \quad \text{(for CT numbers} > 100) \qquad (3.13)$$

In general, one can express the linear attenuation coefficient as

$$\mu = \frac{\rho \cdot N_A \cdot Z}{A}\left(\sigma^e_{coherent}(E,Z) + \sigma^e_{photoeffect}(E,Z) + \sigma^e_{Compton}(E)\right) \qquad (3.14)$$

where $\sigma^e_{coherent}$, $\sigma^e_{Photoeffect}$ and $\sigma^e_{Compton}$ are the coherent (Rayleigh) scattering, photoelectric effect and Compton effect electronic cross sections, E is the effective beam energy, Z is the atomic number of the material, A is the atomic mass, ρ is the mass density and N_A is Avogadro's number. The product ($\rho N_A Z/A$) is defined as the electron density. From Eqs.

3.12, 3.13 and 3.14, a valid relation between the linear attenuation coefficient and the CT number can be calculated for various materials. At megavoltage energies of approximately 10 MV, the relative electron density is almost identical to the relative linear attenuation coefficient because the Compton interaction is dominant at this energy level and is proportional to the electron density.

384 × 384 pixel digitally reconstructed radiographs (DRRs) are computed by projection of the CT data using a summing ray tracing algorithm.[15] Interpolating the DRR to 768 × 768 provides an image that accurately simulates the portal image dimensions with the isocentre position at the centre of our cropped image.

Megavoltage DRR pairs, representing rotated anatomy in the AP and LAT views, are pre-calculated to form our DRR database. Phantom rotations were simulated in steps of 1.5° between -4.5 to 4.5° about the in-plane rotation (*AP*) axis and each out-of-plane rotation axis (superior-inferior (*SI*) and right-left (*RL*)) resulting in 343 megavoltage DRR pairs per simulated isocentre position. The successive rotation matrices adopted in our method are based on the Euler angles to describe rotations from one coordinate system to another, thus ensuring that our DRR data set is complete for any combination of rotation angles. The initial rotation can be taken about any of the three Cartesian axes, and the only limitation is that no two successive rotations can be about the same axis.

The pre-calculated DRR database was used when rotation matching was desired. Since the same DRRs were used throughout rotation matching, and our technique steps through a series of DRRs generated with different in-plane and out-of-plane rotations, the use of a pre-calculated DRR database for rotation matching reduced the computing time by approximately one half, i.e. to approximately 90 minutes.

For translation matching only, DRRs were not pre-calculated because only one DRR is required per view to complete a 3-D translation alignment verification. Using a pre-calculated DRR database for translation matching would save only thirty seconds of computing time per translation alignment verification. For this reason, DRRs for translational matching were calculated only as needed.

3.1.1.4 Image processing environment

The image registration method is implemented using the AVS (Advanced Visual Systems) image processing software[16] running on an Hewlett-Packard 9000 Model 735/125 Unix Workstation.[17] DRRs of 384 × 384 pixels typically require 10 seconds of computing time.

3.1.2 Volume transformation matrix and DRRs

In order to compare DRRs and portal image quantitatively, a common coordinate system must be determined. Two coordinate systems are involved in our image registration process:

1. The world coordinate system or portal image coordinate system
2. The CT-coordinate system

Figure 3.4 schematically illustrates both coordinate systems and show that it is possible to transform the CT-data from the CT-coordinate system to the world coordinate system using a volume transformation matrix (VTM).

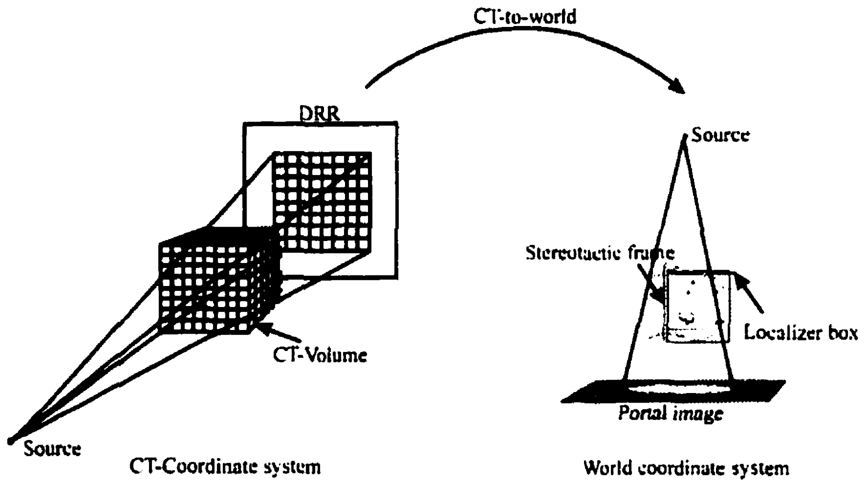

Figure 3.4: In order to compare the data from two different coordinate systems, a common coordinate system must be determined. Using a volume transformation matrix (VTM), it is possible to transform our CT-data from the CT-coordinate system to the world coordinate system.

In order to simulate DRRs that correspond to portal images acquired at various beam-to-patient geometries, the CT-data must be manipulated to simulate head displacements in world coordinates.

In general, a vector in one coordinate system can easily be transformed into an equivalent vector in another coordinate system. Such a transformation can be expressed as:

$$x' = x[A] \tag{3.1}$$

where x is a vector in a coordinate system and x' is the corresponding vector in the second coordinate system. The matrix $[A]$ is defined as the transformation matrix. The reverse process can also be done, i.e. the vector x' can be expressed in terms of the first coordinate system by simply multiplying x' by the inverse of the transformation matrix. Using this simple transformation analogy, it is possible to determine a VTM capable of transforming the CT-data into world coordinates. In order to simulate DRRs that correspond to portal images obtained in the world coordinate system, the complete CT-volume must be transformed to the world coordinate system, where the world coordinate is defined as the patient position on the linac treatment couch. To determine the world coordinates used to create the best matching DRRs, the CT-to-world VTM must be quantified in terms of translations in the x, y and z Cartesian planes, gantry rotation angle, couch tilt angle and couch rotation angle. Sherouse et al developed a method for relating any displacements in world coordinates to a series of transformation matrices defining all possible translations and rotations.[18] The overall transformation in world coordinates is defined as

$$F = SI \cdot AP \cdot RL \cdot T_{xyz} \tag{3.2}$$

where F is the overall transformation matrix, T_{xyz} is the x, y, and z translation matrix and SI, AP *and* RL are the superior-inferior, anterior-posterior and right-left rotation matrices respectively:

$$T_{xyz} = \begin{bmatrix} 1 & 0 & 0 & T_X \\ 0 & 1 & 0 & T_Y \\ 0 & 0 & 1 & T_Z \\ 0 & 0 & 0 & 1 \end{bmatrix} \tag{3.3}$$

$$SI = \begin{bmatrix} \cos(\theta) & 0 & -\sin(\theta) & 0 \\ 0 & 1 & 0 & 0 \\ \sin(\theta) & 0 & \cos(\theta) & 0 \\ 0 & 0 & 0 & 1 \end{bmatrix} \tag{3.4}$$

$$AP = \begin{bmatrix} \cos(\phi) & \sin(\phi) & 0 & 0 \\ -\sin(\phi) & \cos(\phi) & 0 & 0 \\ 0 & 0 & 1 & 0 \\ 0 & 0 & 0 & 1 \end{bmatrix} \tag{3.5}$$

$$RL = \begin{bmatrix} 1 & 0 & 0 & 0 \\ 0 & \cos(\varphi) & \sin(\varphi) & 0 \\ 0 & -\sin(\varphi) & \cos(\varphi) & 0 \\ 0 & 0 & 0 & 1 \end{bmatrix} \tag{3.6}$$

where *Tx*, *Ty* and *Tz* are the x, y and z translations, respectively, and θ, ϕ and φ are the rotation angles around the *SI*, *AP* and *RL* rotation axes respectively. The transformation from the CT-coordinate system to the world coordinate system may be expressed as:

$$x' = x \cdot F \tag{3.7}$$

where x is of the form

$$x = [x_1, x_2, x_3, 1] \tag{3.8}$$

The successive rotation matrices adopted in our method are based on the Euler angles to describe rotations from one coordinate system to another. This approach ensures that our DRR data set is complete for any combination of rotation angles. It is important to note that the sequence of rotations used to define the final orientation of the coordinate system is, to some extent, arbitrary. The initial rotation can be taken about any of the three Cartesian axes. In the subsequent two rotations, the only limitation is that no two successive rotations can be about the same axis.

The DRR calculation algorithm uses the overall transformation matrix F to position the CT-data in the world coordinate simulating the patient's head at a given orientation in world coordinates. The summing ray tracing process is applied to the CT-data to create AP and LAT DRRs. DRRs can be created to simulate any desired orientation of the patient's head in world coordinates.

3.1.3 Selecting the region of interest

As discussed in Chapter 2, the correlation algorithm requires a search mask and a search image. A 64 × 64 region of interest is selected from the AP and LAT portal images. To obtain an accurate match, the search mask must contain a noticeable anatomical feature that appears in both the portal image and the corresponding DRR. The DRR search image is then cropped to a 256 × 256 search window centered at the selected anatomical feature in order to maximize the probability of a successful match.

3.1.4 Image correlation

When the portal search mask and the DRR search window are properly selected in the AP and LAT views, the image correlation algorithm is applied using the FFT implementation of Pearson's correlation coefficient that we described in Chapter 2. The search mask is compared throughout the corresponding DRR search window. As the search masks sweeps the search image, a correlation value is outputted for every position (m,n), thus forming a 2-D correlation matrix for the AP and LAT views. Two typical correlation matrices are displayed in Figs. 3.5 and 3.6 resulting from correlating the search mask and search image in AP and LAT views respectively. From these figures, one can see that the maximum correlation coefficient reveals the position (in pixels) of the best match between the search mask and search window.

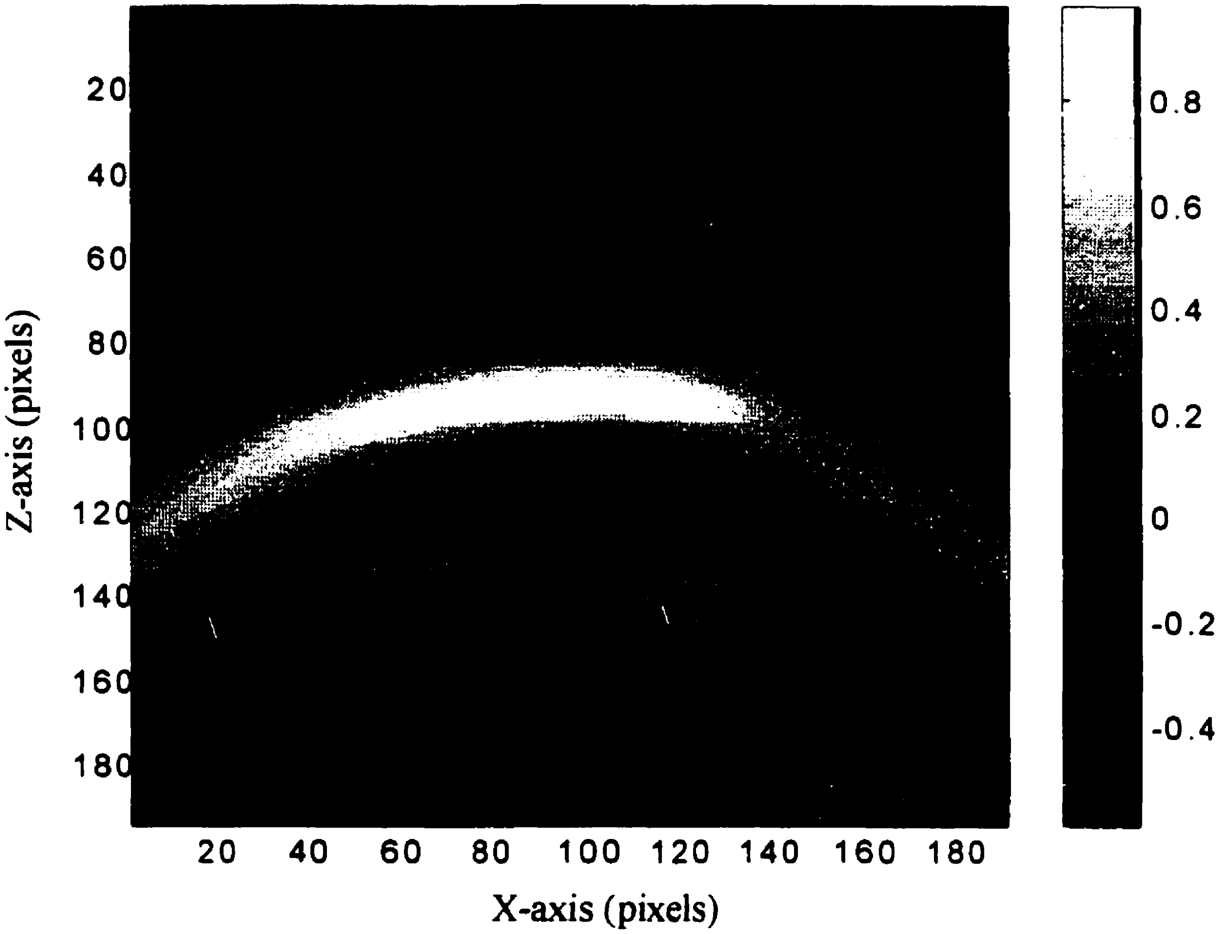

Figure 3.5: 2-D correlation matrix resulting from correlating the AP portal search mask with the AP DRR search window. The location where the search mask best matches the search window is represented by the location of the maximum correlation coefficient. The intensity of each pixel represents the correlation value at that point.

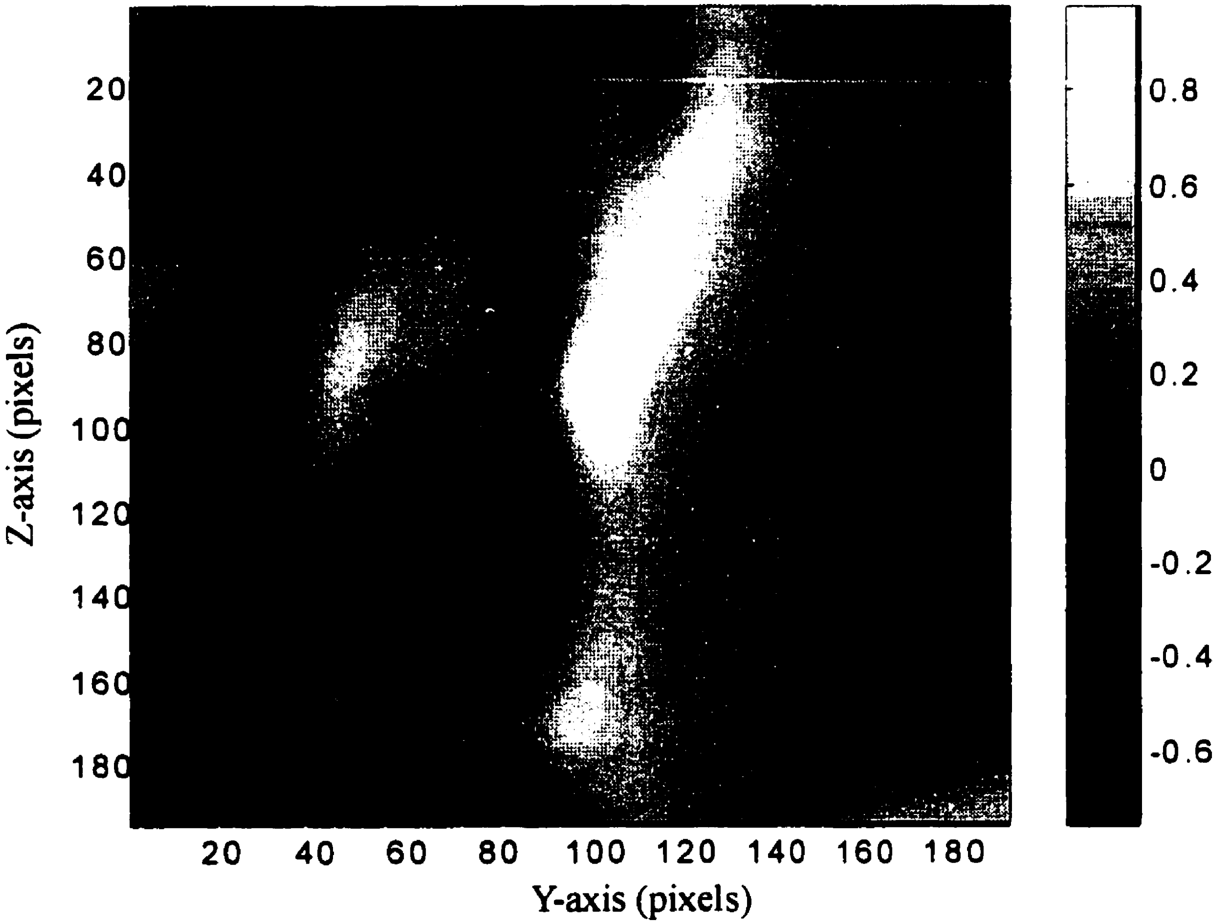

Figure 3.6: 2-D correlation matrix resulting from correlating the LAT portal search mask with the LAT DRR search window. The location where the search mask best matches the search window is represented by the location of the maximum correlation coefficient. The intensity of each pixel represents the correlation value at that point.

To appreciate the response of the correlation algorithm when it correlates the search mask with the search window, 3-D representations of Figs. 3.5 and 3.6 are shown in Figs. 3.7 and 3.8 respectively. The 3-D representations clearly show that even though several local *minima* and *maxima* are present, the overall maximum correlation value can easily be determined. This particular aspect renders Pearson's correlation coefficient ideal for image registration purposes.

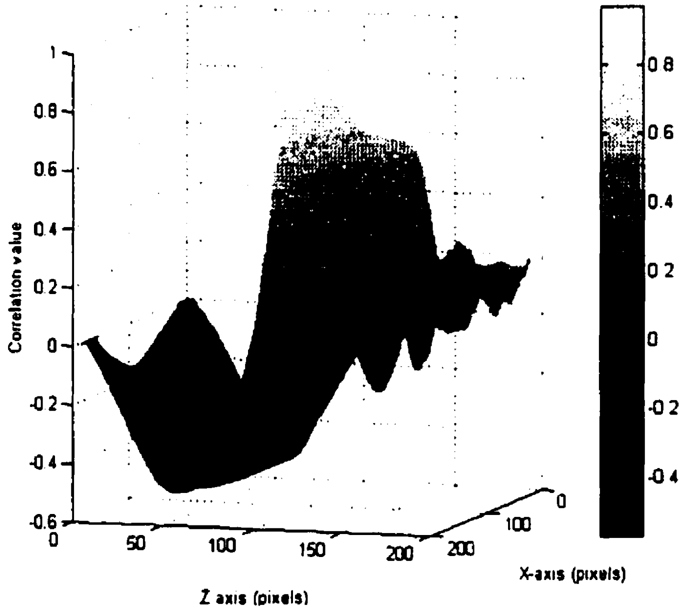

Figure 3.7: 3-D representation of the correlation matrix resulting from correlating the AP portal search mask with the AP DRR search window. Although several local minima and maxima are typically observed in the correlation matrix, the overall maximum correlation value clearly stands out and enables us to detect it's position in the 2-D matrix.

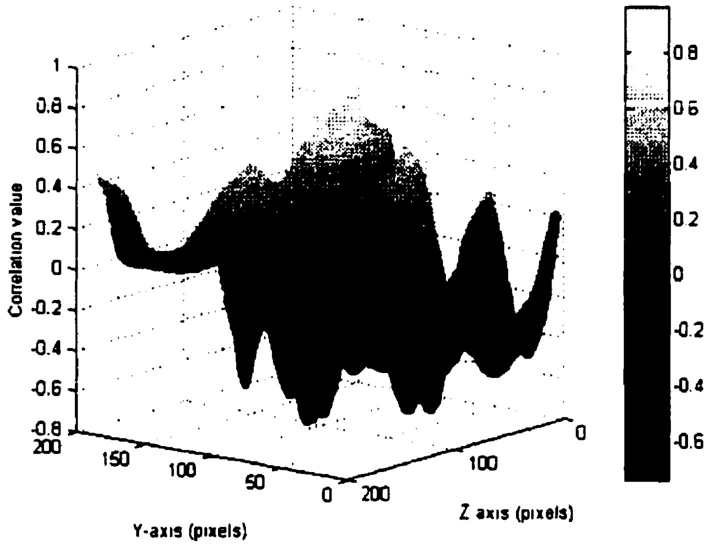

Figure 3.8: 3-D representation of the correlation matrix resulting from correlating the LAT portal search mask with the LAT DRR search window. Although several local minima and maxima are typically observed in the correlation matrix, the overall maximum correlation value clearly stands out and enables us to detect it's position in the 2-D matrix.

3.1.5 Interpretation of maximum correlation coefficient

Each time a portal image search mask is compared throughout a corresponding DRR search window, the output is a correlation matrix where each correlation value describes how well the portal image region of interest resembled the DRR at a given position (m,n). The highest correlation value is indicative of the position of the best match of the portal image search mask within the DRR search image.

3.1.5.1 Detecting translation positioning errors

A translation positioning error is quantified by counting the number of pixels between the position of the expected position and the position of the highest correlation value along the x, y and z axes. The expected matching position is obtained during the search mask selection. Theoretically, the position of the maximum correlation coefficient obtained after correlating the search mask with the search image should be identical to the location of the centre of the search mask in the reference image (in pixels). Any discrepancies reveal translation positioning errors. Multiplying the error in pixels by the pixel size of the DRR search image will give us the error in units of distance, usually in millimeters. However, one must consider that this translation positioning error is determined at the imaging plane. We wish to obtain the translation positioning error relative to the isocentre. As illustrated in Fig. 3.9, any displacement along the axis perpendicular to the imaging plane will change the projection of any displacement parallel to the imaging plane. This 2-D example can be expressed in the following relations:

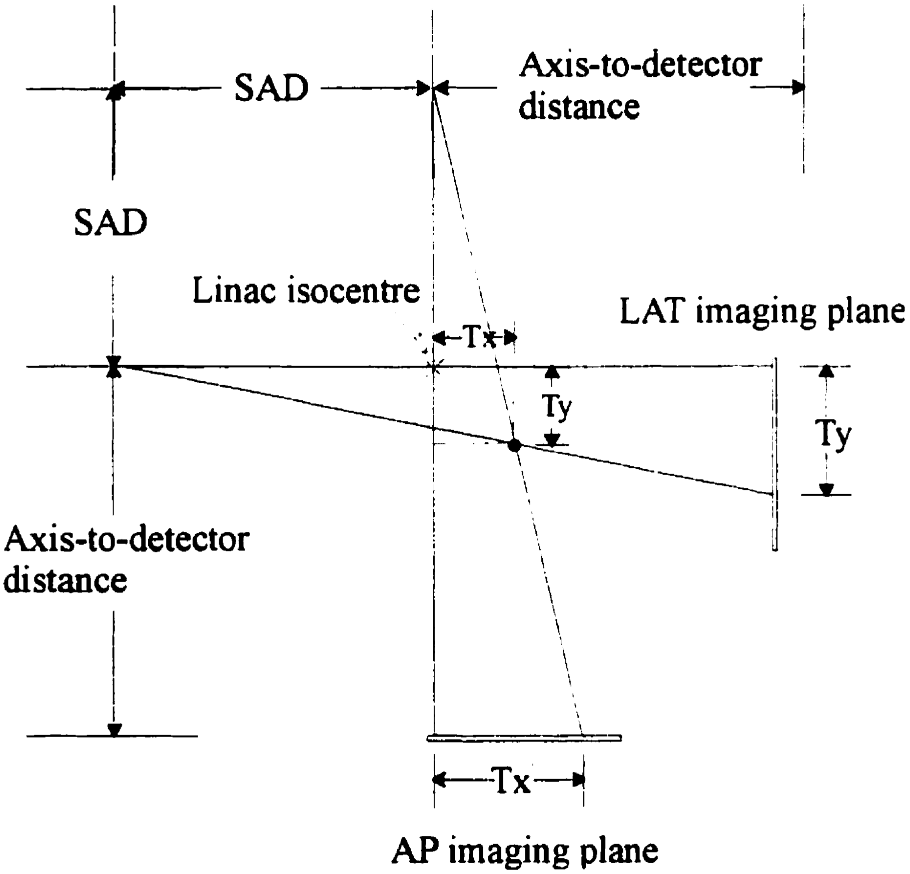

Figure 3.9: Schematic illustration of the orthogonal imaging acquisition set-up. It becomes evident that a displacement along Ty will affect the projected magnification of the Tx displacement and vice versa.

$$\frac{Tx'}{Tx} = \frac{source\text{-}to\text{-}detector\ distance}{SAD + Ty} \tag{3.9}$$

$$\frac{Ty'}{Ty} = \frac{source\text{-}to\text{-}detector\ distance}{SAD + Tx} \tag{3.10}$$

where Tx an Ty are the translations incurred at the isocentre by the target along the x and y axes respectively, and Tx' and Ty' are the respective projections of the Tx and Ty displacements at the imaging plane. After the image registration procedure, we obtain Tx' and Ty' in pixels, from which we can determine Tx and Ty. However, a careful inspection of the Eqs. 3.9 and 3.10 reveal that no significant error is introduced when neglecting the displacement along the axis perpendicular to the imaging plane. For example, with typical values of SAD = 100 cm, source-to-detector distance = 140 cm, $Tx' = 1$ cm and $Ty' = 1$ cm, we obtain a difference of 0.010 mm between the Tx and Ty values calculated with those calculated without correction for the displacement along the axis perpendicular to the imaging plane. Therefore, one can safely assume that negligeable error is introduced by neglecting the magnification effects of displacements along the axis perpendicular to the imaging plane, thus simplifying the direct calculation of translation errors.

3.1.5.2 Detecting rotation positioning errors

Rotation positioning errors can also be detected with the FFT implementation of Pearson's correlation coefficient. DRRs are generated for a series of different combinations of in-plane and out-of-plane orientations. Each DRR search window is correlated with the portal image search mask, outputting a 2-D correlation matrix for each DRR in each view. For the AP and LAT views, the maximum correlation coefficient from each 2-D correlation matrix is determined. In-plane and out-of-plane rotation positioning errors are revealed by comparing the actual treatment set-up angles (gantry rotation angle, table rotation angle and table tilt rotation angle) with the DRR rotation parameters that produce the correlation matrices with the maximum overall correlation coefficient in the AP and LAT views.

3.2 REFERENCES

[1] K. Otto and B. G. Fallone, "Frame slippage verification in stereotactic radiosurgery," Int. J. Radiat. Oncol. Biol. Phys. 41, 199-205 (1998).

[2] D. H. Hristov and B. G. Fallone, "A grey-level image alignment algorithm for registration of portal images and digitally reconstructed radiographs," Med. Phys. 23, 75-84 (1996).

[3] 3M diagnostic head phantom, 3M Corporation, St. Paul, Minnesota.

[4] Leksell Stereotactic Frame, Elekta Instrument AB, Stockholm, Sweden.

[5] R. Siddon, "Solution to treatment planning problems using coordinate transformations," Med. Phys. 8, 766-774 (1981).

[6] Clinac 18 linear accelerator, Varian Associates, Palo Alto, California.

[7] X-Omatic radiation therapy cassette, Eastman Kodak Co., Rochester, New York.

[8] E. I. Du Pont de Nemours & Co. Inc. Wilmington, Delaware.

[9] M. Goitein, M. Abrams, D. Rowell, H. Pollari, and J. Wiles, "Multi-dimensional treatment planning: beam's eye view, back projection, and projection through sections," Int. J. Radiat. Oncol. Biol. Phys. 9, 789-797 (1983).

[10] H. E. Johns and J. R. Cunningham, "The Physics of Radiology," fourth edition, 796 (1983).

[11] R. P. Parker, P. A. Hobday, and K. J. Cassell, "The direct use of CT numbers in radiotherapy dosage calculations for inhomogeneous media," Phys. Med. Biol. 24, 802-809 (1979).

[12] C. Constantinou, J. C. Harrington, and A. DeWerd, "An electron density calibration phantom for CT based treatment planning computers," Med. Phys. 19, 325-327 (1992).

[13] E. C. McCullough and T. W. Holmes, "Acceptance testing computerized radiation treatment planning systems: Direct utilization of CT scan data," Med. Phys. 12, 237-242 (1985).

[14] E. Orfali, "Verification of a 3D external photon beam treatment planning system," McGill University, M.Sc. dissertation (1996).

[15] M. Garity, "Ray tracing irregular volume data. Proceedings of the 1990 San Diego Workshop on Volume Visualization," Computer Graphics 24, 35-40 (1990).

[16] Advanced Visual Systems, Waltham, Massachusetts.

[17] HP 9000 P 735/125 Workstation, Hewlett-Packard Company, Palo Alto, California.

[18] G. W. Sherouse, "Coordinate transformations as a primary representation of radiotherapy beam geometry," Med. Phys. 19, 175-179 (1992).

Chapter 4:

Results

4.1 DRR-TO-DRR MATCHING

4.1.1 Translation error registration

DRR-to-DRR matching serves as validation for our method. The first DRR-to-DRR matching test steps through a series of matching tests where the search image that have been translated along the x, y and z axes by known amounts are registered with a zero displacement reference image. A total of eight different 64 × 64 search masks, four in the AP view and four in the LAT view, were chosen to include four anatomical features from each view from zero displacement DRR reference images. To obtain an accurate match, the search mask must contain a noticeable anatomical feature that appears in both the portal image and the corresponding DRR. Figures 4.1 and 4.2 illustrate typical anatomical features, each of which was used for matching. For the AP view, they are the upper-left bony orbit, the sagital suture, the upper-right bony orbit and the nasal bone, which are features 1, 2, 3, and 4, respectively. Similarly, for the LAT view, they are the right bony orbit, the petrous bone, the external occipital protuberance and the upper coronal suture, which are features 5, 6, 7 and 8 respectively. Each search mask was compared with 1331 pairs of test images generated with the following parameters: Tx, Ty, Tz = -15 mm to +15 mm (in steps of 3 mm), AP, SI, RL = 0 degrees. We defined Tx, Ty and Tz as the *translation* errors introduced along the x, y and z axes respectively, and AP, SI, RL as the *rotation* errors introduced around the anterior-posterior, superior-inferior and right-left *rotation* axes, respectively. The test was repeated for each of the search masks and revealed the sensitivity of our method to variations in *translations* along each translation axis. Experimental results are presented in Fig. 4.3. The points in the figure represent the mean deviation between the correct position and the one given by the registration algorithm during DRR-to-DRR matching for each of the eight features. The error bars show the standard deviation obtained with the data set for each feature. As shown in Fig. 4.3, for DRR-to-DRR translation registration, the image registration process is capable of determining the *translation* deviations to well within 0.8 mm of the correct value with an average of 0.58 mm and a mean radial registration error of 0.97 mm.

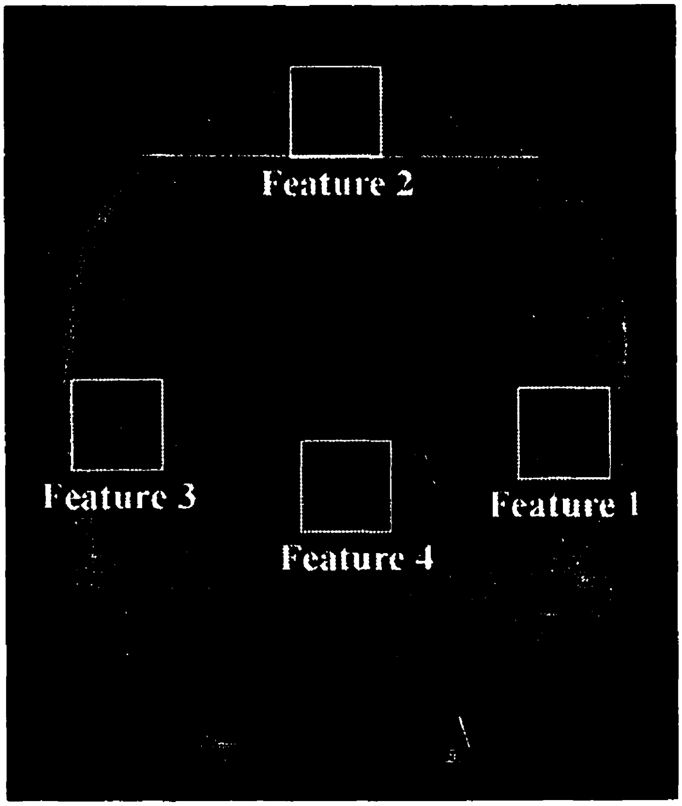

Figure 4.1: AP DRR illustrating the four search masks selected for DRR-to-DRR image registration.

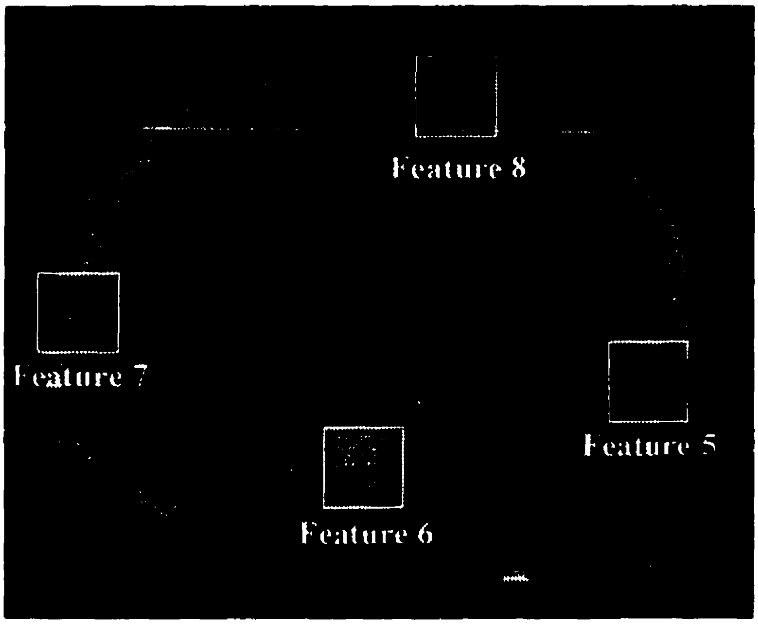

Figure 4.2: LAT DRR illustrating the four search masks selected for DRR-to-DRR image registration.

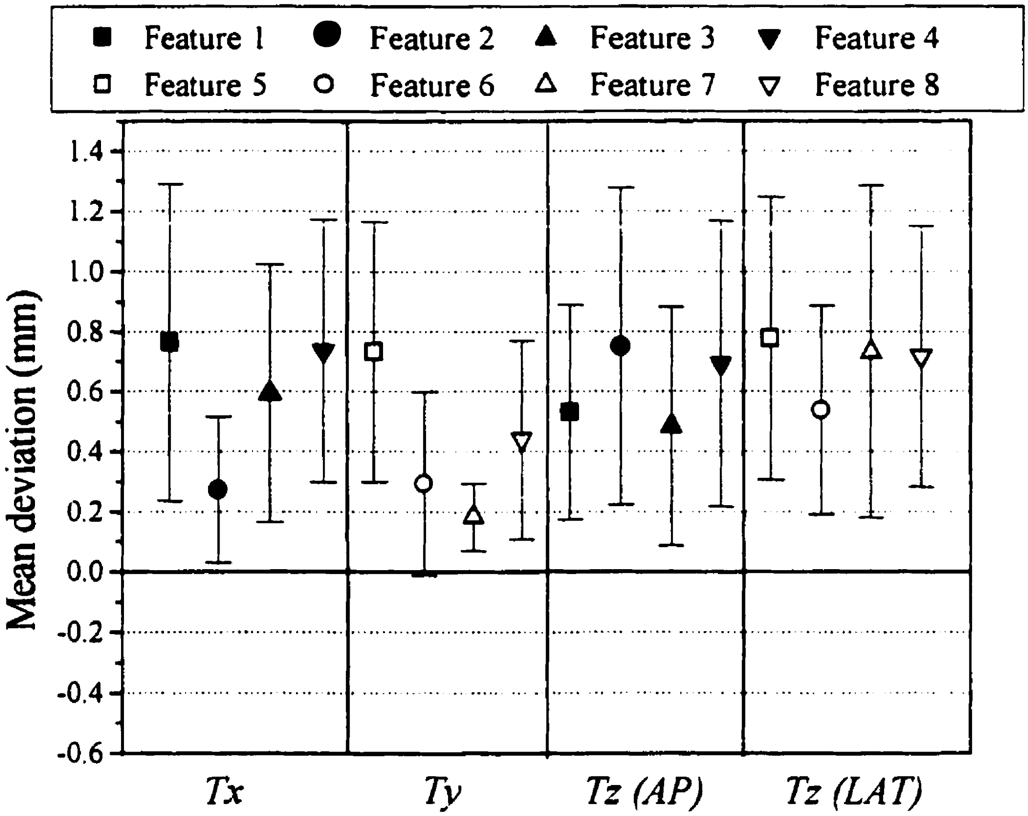

Figure 4.3: Results of DRR-to-DRR translation registration tests. Plotted are the mean and standard deviations between the actual positions and the ones given by the registration algorithm during registration along the Tx, Ty and Tz translation components. Each point is the result of the registration of a zero displacement DRR and 1331 randomly generated DRRs not exceeding ± 15 mm from the actual position.

4.1.2 Combined rotation and translation error registration

Although all eight features may provide relatively accurate results for *translation* matching, they do not all allow our algorithm to discriminate between combined *rotations* and *translations* or even between the different rotation axes. The same eight search masks used for *translation* matching were then compared with 15 AP and LAT test images generated at: *AP*, *SI*, *RL* = -4.5° to 4.5° in steps of 1.5° at 15 arbitrary *Tx*, *Ty* and *Tz* values. Only features 2, 5 and 6 allowed discrimination between *rotations*. Figure 4.4 shows the mean differences between the correct translation and rotation parameters, and those provided by our registration algorithm using the feature pairs 2 and 5, and 2 and 6. Figure 4.4 allows a comparison of the alignment errors obtained with each feature pairs, from which we can conclude that features 2 and 6 are better suited for determining *translation* alignment errors while features 2 and 5 are be better suited for determining *rotation* alignment errors. A direct comparison of the mean differences between the correct *rotation* alignment and the one provided by the registration algorithm using features 2, 5 and 6 is presented in Fig. 4.5, and reveals that feature 5 proves to be more accurate for detecting in-plane and out-of-plane *rotations*. However, feature 6 proved to be better for *translation* registration (see Fig. 4.3). In-plane and out-of-plane rotation errors are detected with an average accuracy of 0.79°.

To quantitatively compare these results and to determine which pairs of features is better for overall position verification, we introduced a method that enables us to directly compare the effects of combined *rotations* and *translations*. For this purpose, 4000 points were randomly selected throughout a simulated spherical tumor volume with a 2 cm radius. The points were then subjected to the same *rotations* and *translations* of the best matching DRRs given by the image registration results using the features pairs. Since the actual orientation of the DRR is known, the radial distance *r* between the correct position of each point and the position of each point in the tumor at the orientation given by the registration algorithm can be determined. Smaller radial *translation* errors are obtained with feature 2 and 6 than with features 2 and 5 (r = 1.64 mm versus r = 1.88 mm).

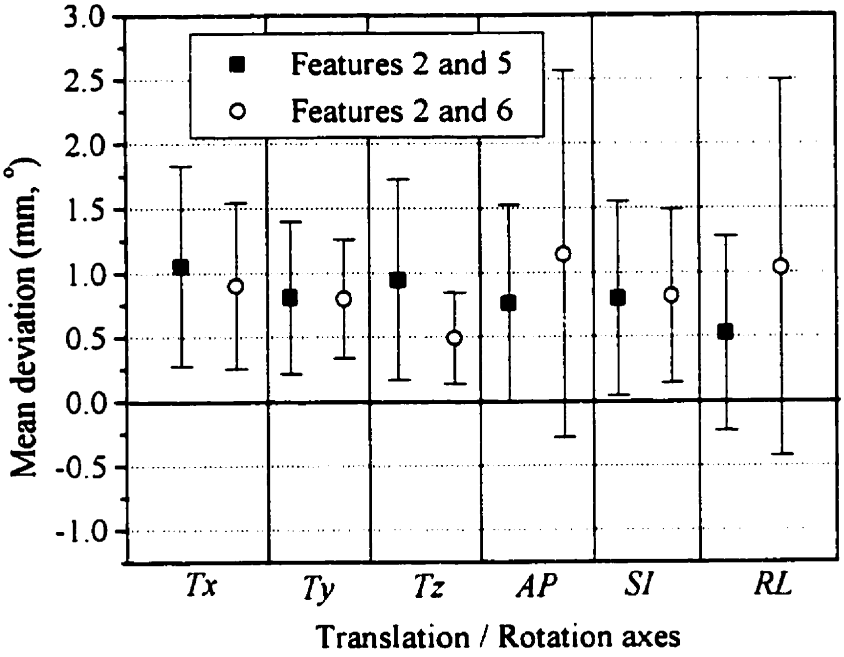

Figure 4.4: Results of DRR-to-DRR translation and rotation registration tests. Plotted are the mean and standard deviations between the actual alignment and the one given by the registration algorithm during registration along the Tx, Ty and Tz translation axes and AP, SI and RL rotation axes. Each point is the result of the registration of a zero displacement DRR and 343 randomly generated DRRs not exceeding ± 15 mm for translation and ± 4.5° for rotations from the actual alignment.

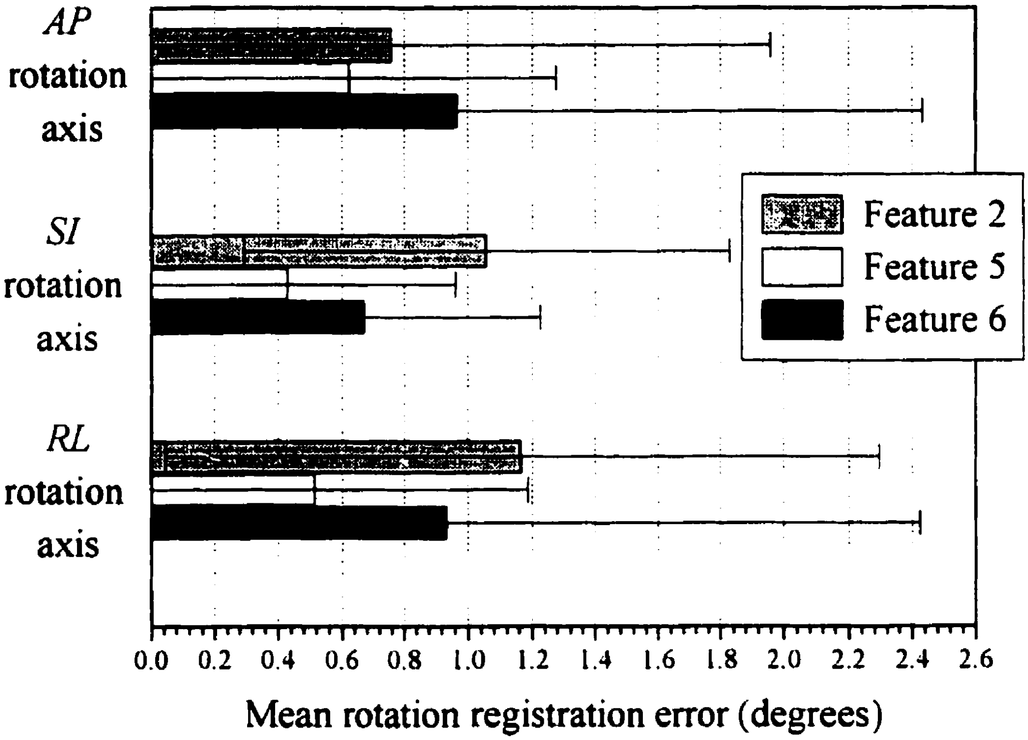

Figure 4.5: Results of DRR-to-DRR translation and rotation registration tests. Plotted are the mean differences and standard deviations between the correct rotation alignment and the rotation alignment given by the registration algorithm using features 2, 5 and 6 along the AP, SI and RL rotation axes.

4.1.3 Correlation coefficient behavior

Figures 4.6 and 4.7 show the typical behavior of the maximum correlation coefficient as a function of translation displacements along the imaging plane for features 2 and 6. The overall maximum correlation coefficient of unity is, as expected, obtained when the search image is identical to the reference image. As the CT-volume is displaced, the search image's isocentre is displaced accordingly and the new DRR image is slightly changed because of the beam divergence. As expected, the maximum correlation coefficient does drop slightly. In general, we noticed that the drop in the maximum correlation coefficient is more pronounced for displacements along the z-axis, probably caused by the gap between slices during the acquisition of the CT-volume.

To analyze the effect of magnification on the maximum correlation coefficient, the behavior of the maximum correlation coefficient was monitored for different displacements along the axis perpendicular to the imaging plane. Figures 4.8, 4.9, 4.10 and 4.11 illustrate magnification effects for features 2 and 6 in the AP and LAT views respectively using magnification factors of 0.85, 1.0 and 1.15. As expected, the maximum correlation coefficient does drop slightly when magnification is introduced in the search image.

Even though changes in beam divergence and magnification affect the maximum correlation value, we expect our method to be able to discriminate between translation and rotation alignment errors.

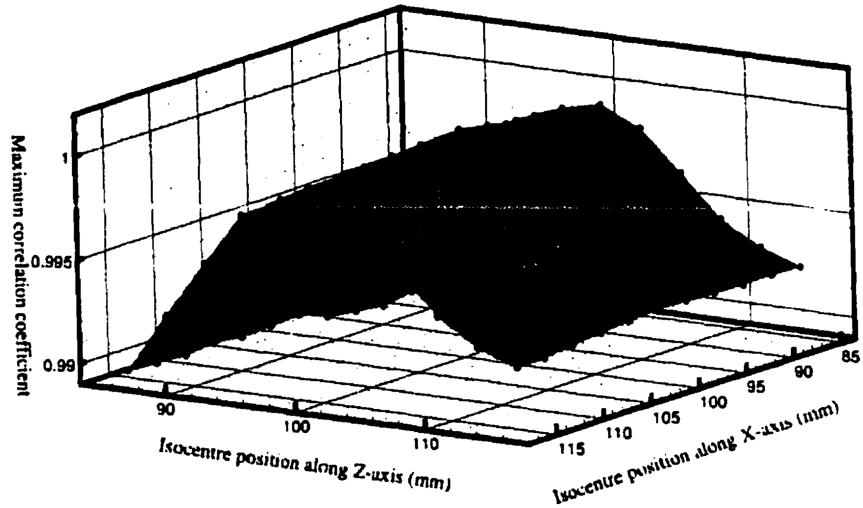

Figure 4.6: Maximum correlation coefficient as a function of translations along the x and z stereotactic axes for feature 2 (AP view).

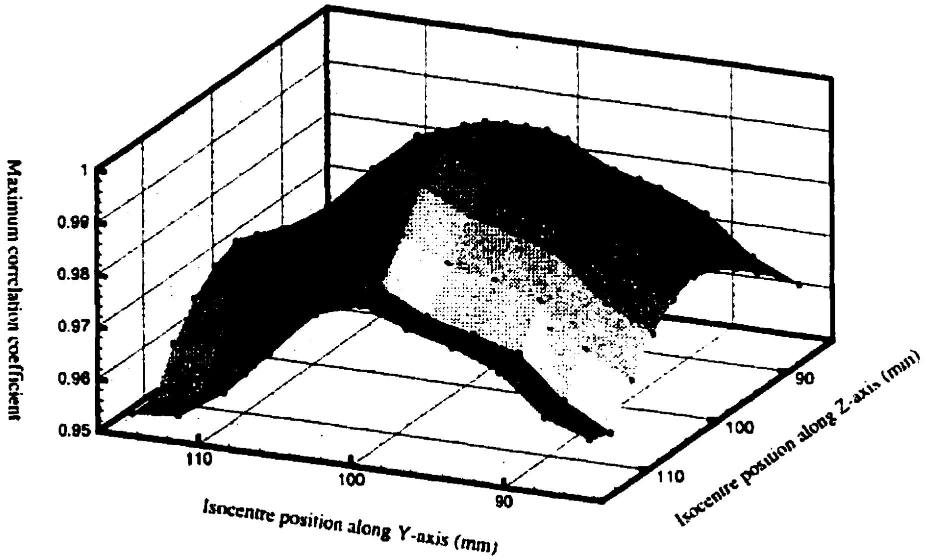

Figure 4.7: Maximum correlation coefficient as a function of translations along the y and z axes for feature 6 (LAT view).

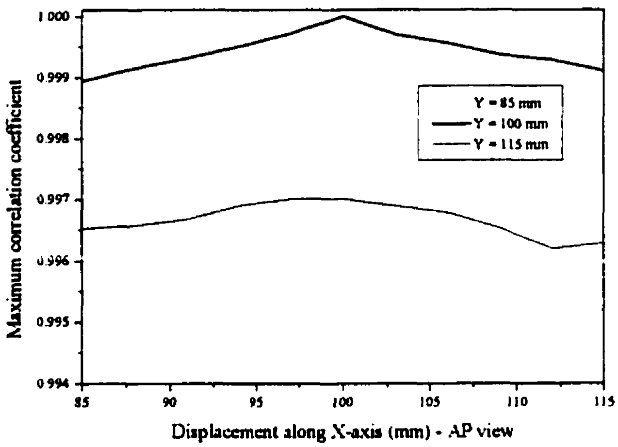

Figure 4.8: *Maximum correlation coefficient as a function of in-plane displacements along the x-axis measured at different displacements along the y-axis (perpendicular to the imaging plane) for feature 2 in the AP view.*

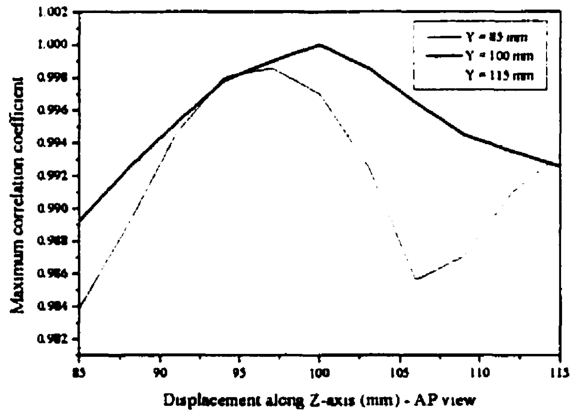

Figure 4.9: *Maximum correlation coefficient as a function of in-plane displacements along the z-axis measured at different displacements along the y-axis (perpendicular to the imaging plane) for feature 2 in the AP view.*

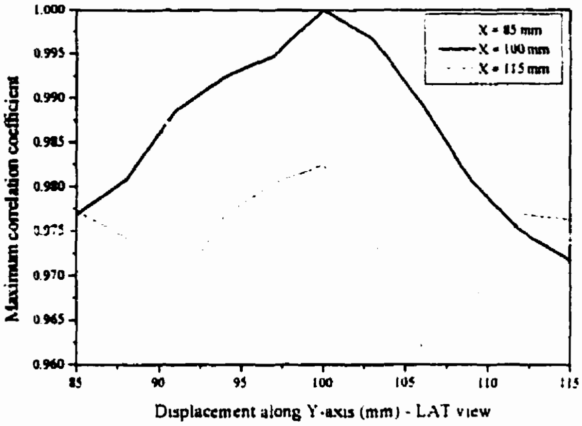

Figure 4.10: Maximum correlation coefficient as a function of in-plane displacements along the y-axis measured at different displacements along the x-axis (perpendicular to the imaging plane) for feature 6 in the LAT view.

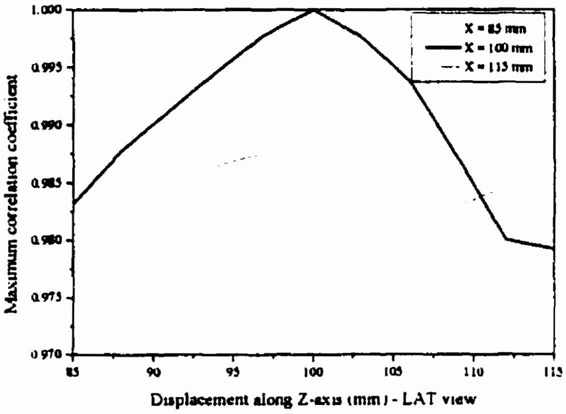

Figure 4.11: Maximum correlation coefficient as a function of in-plane displacements along the z-axis measured at different displacements along the x-axis (perpendicular to the imaging plane) for feature 6 in the LAT view.

4.2 PORTAL-TO-DRR MATCHING

4.2.1 Translation error registration

Portal-to-DRR matching serves as a feasibility test for our method in clinical conditions. Three portal images of the head phantom were acquired and digitized. Because they were deemed best for matching in Sec. 4.1, two search masks, containing features 2 and 6, were selected from each AP and LAT portal image. The portal image search masks were compared with a series of DRRs generated at 375 random *Tx*, *Ty* and *Tz* displacements between -15 mm and +15 mm in steps of 5 mm along each axis. The maximum correlation allowed us to determine the accuracy with which the portal-to-DRR matching process is able to determine the *translations* given to the DRR. This is repeated for a series of 375 DRR displacements in the AP and LAT views and results are presented in Fig. 4.12. For translations only, the mean translation registration error is 1.22 mm, and the mean radial registration error is 2.14 mm.

4.2.2 Combined rotation and translation error registration

To verify the accuracy of the method for determining total errors combining *translations* with in-plane and out-of plane *rotation* errors in the portal image, DRRs were created at different combinations of in-plane and out-of-plane *rotations* at 15 random *Tx*, *Ty* and *Tz* isocentre position. The same portal image search masks from the previous section were compared with the pre-calculated megavoltage DRR database. The following *rotation* parameters were used to generate the pair of orthogonal AP and LAT DRRs: *AP*, *SI* and *RL* = -4.5° to 4.5° in steps of 1.5°. Figure 4.13 shows the mean differences between the expected *translation* and *rotation* alignment parameters and those provided by our registration algorithm using features 2 and 6. In-plane and out-of-plane *rotation* errors are detected with an average accuracy of 1.31°.

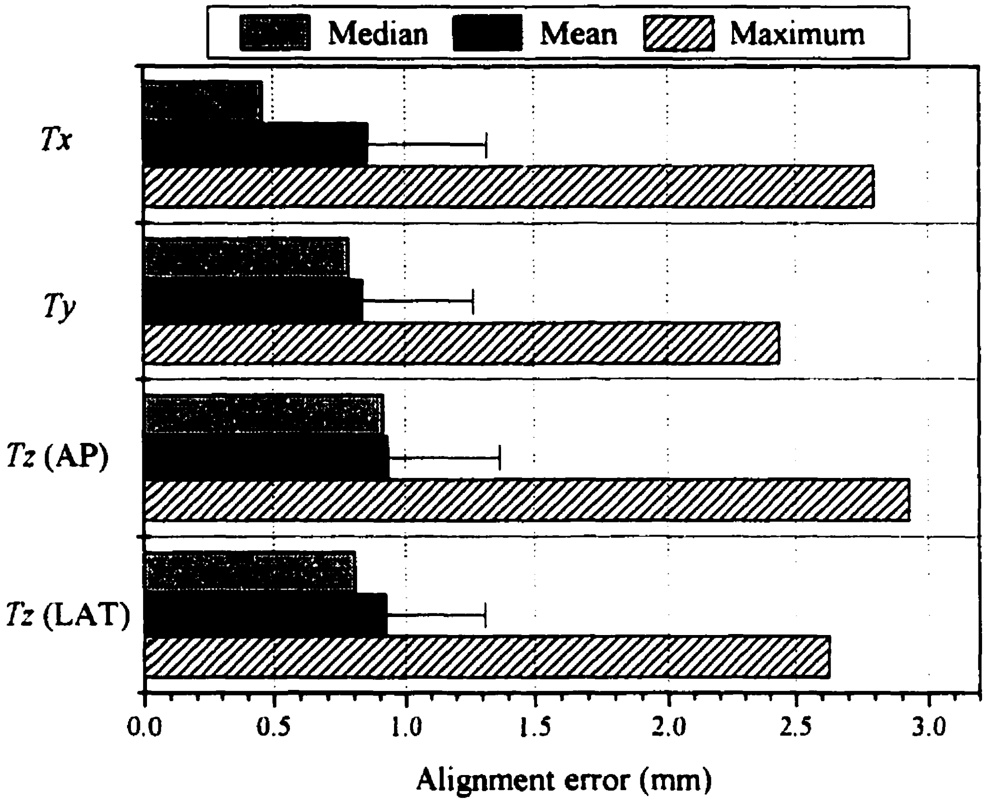

Figure 4.12: Results of portal-to-DRR translation registration tests. Plotted are the maximum, mean and median alignment errors between the correct alignment and the alignment given by the registration algorithm with 3 pairs of orthogonal portal images and 375 DRR pairs simulated at random Tx, Ty and Tz isocentre positions within ± 15 mm of the correct position. The error bars represent the standard deviation.

Using the same 2 cm radius spherical tumor simulations, described in Sec. 5.1, we evaluated the total radial displacement for the portal-to-DRR registration data set. Results are presented in Fig. 4.13. For portal-to-DRR registration, the mean radial registration error, which included *translation* and *rotation* errors, is 2.74 mm.

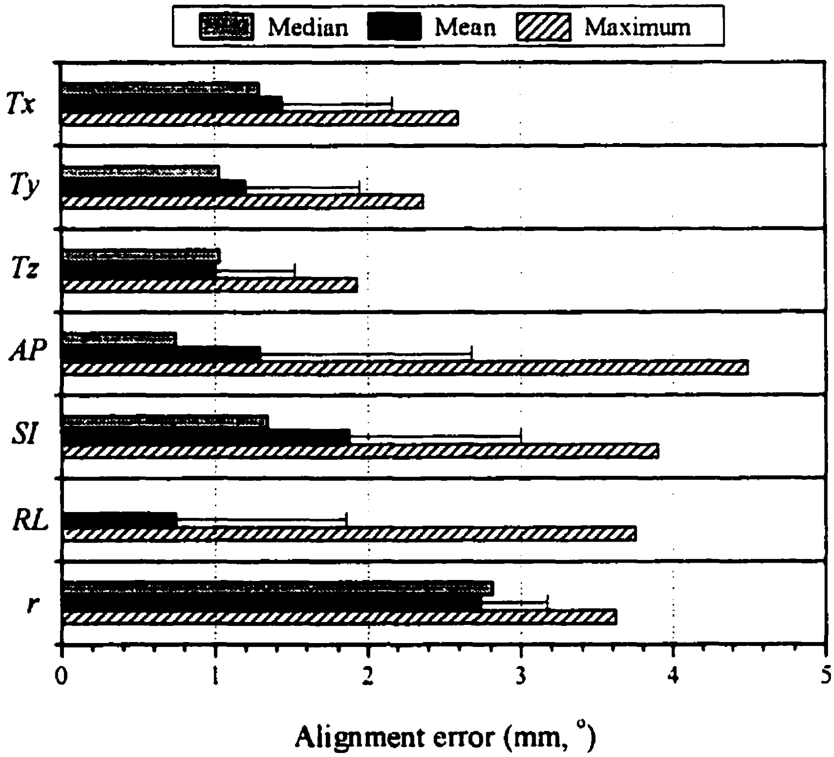

Figure 4.13: Results of portal-to-DRR translation and rotation registration tests. Plotted are the maximum, mean and median alignment errors between the correct alignment and the alignment given by the registration algorithm with 3 pairs of orthogonal portal images and 15 DRR pairs simulated at random Tx, Ty and Tz within ± 15 mm of the correct position. The error bars represent the standard deviation

Chapter 5:

Discussion and Conclusion

5.1 SUMMARY

We developed an automatic, anatomy-based, image registration method for detecting translation, in-plane and out-of-plane rotation errors using a correlation-based approach. The advantages of this technique is that it requires no user-delineation of anatomical features, it is robust for cases where the images have undergone intensity changes, it does not require identification or delineation of fiducial landmarks and requires no user-intervention other than image acquisition and processing.

As Hristov and Fallone describe, the normalized correlation coefficient is invariant under scaling of the image intensities, but Pearson's correlation coefficient is invariant under scaling and shifting of image intensities.[1] Insensitivity to image variations is an important factor because detector response and dose delivery can vary significantly from one treatment to another. Pearson's correlation coefficient is robust when encountering in-phantom scatter in portal images.[1] No anatomy delineation, edge enhancements or point pair matching is required in the search mask or search image when using a correlation approach. This eliminates most of the user error and inter-user variability encountered in many other anatomy-based, image registration methods.

The algorithm was very efficient for determining any translation errors (typically 7 seconds per view on our system). For DRR-to-DRR registration, the mean translation registration error is 0.58 mm. For translations only, the mean radial registration error is 0.97 mm. In-plane and out-of-plane rotation errors are detected with an average accuracy of 0.79°. For DRR-to-DRR registration, which include both rotational and translational errors, the mean radial registration error is 1.55 mm.

For portal-to-DRR registration, the mean translation registration error is 1.22 mm. For translations only, the mean radial registration error is 2.14 mm, which is comparable to the level of accuracy obtained with 3-D methods that involve manual intervention,[2,3] inconsistent anatomy extraction,[4] or diagnostic images.[5,6] In-plane and out-of-plane rotation errors are detected with an average accuracy of 1.31°. For portal-to-DRR registration, which include both rotational and translational errors, the mean radial registration error is 2.74 mm. In its present form, the correlation algorithm requires 7 seconds per angle combination per view with pre-calculated DRRs, thus requiring approximately 90 minutes for one clinical case.

The performance of the algorithm depends on the ability of the operator to select a valid anatomical feature. This is especially true for portal-to-DRR matching considering the quality of the portal images. The portal-to-DRR experimental results are higher than what we obtained during DRR-to-DRR trials, which was expected because of the poor quality of portal images. The surgical collimator, the head fixation device and stereotactic frame increase the level of scatter in the image and leads to certain artifacts than can affect the quality of the registration. Portal image quality could be improved by employing improved electronic portal images or better portal films, such as the Kodak ECL portal film. Better quality portal images would also produce more accurate results during image registration.

Studies with portal films show that the standard deviation in treatment-to-treatment variation in patient set-up position is 3 mm.[7] This deviation does not vary significantly for different treatment sites. However, for brain, the average discrepancy between portal and simulator films is 5 mm. Although immobilization devices, such as stereotactic frames, reduce treatment set-up positioning errors, a stereotactic radiosurgery report reveals that the total uncertainty in treatment delivery and target localization is from 2.4 mm to 3.7 mm.[8] The accuracy of our 3-D anatomy-based automatic image registration method lies within these values. Although our method was not tested for the pelvic region, it could easily be implemented since it uses constant size search masks, which makes it independent of field sizes.

5.2 FUTURE WORK

A potential improvement to the technique would be to incorporate a minimization algorithm that maximizes the correlation value during registration to ensure convergence of the correlation peek during in-plane and out-of-plane rotation registration. This would reduce the number of iterations involved, thus reducing the computing time. In addition, it would improve the accuracy of the system for rotation registration. Presently, DRRs are generated at pre-determined intervals of in-plane and out-of-plane rotations, thus probably missing the actual overall maximum correlation coefficient. The algorithm may be detecting local *maxima* that may be significantly different from the actual orientation of the portal image. A minimization algorithm would assure convergence to the overall maximum correlation coefficient. Fast Annealing and Genetic Algorithms[9] search thoroughly for the overall maximum in order to guarantee convergence, but the amount of iterations involved render these algorithms impractical.[1,6] Numerous authors describe implementations Brent's method[1] and Powell's multidimensional direction set method[6] for assuring convergence of image registration cost-functions. Implementing such algorithms during rotational registration would maximize the convergence and reduce the number of time-consuming portal-to-DRR registrations involved.

In addition to a minimization algorithm, we propose incorporating the histogram-shifting algorithm (HS) developed at our institution.[10] This particular algorithm is based on local histogram modification resulting in the detection and/or enhancement of edges within the image while minimizing the artifact creation and noise amplification encountered in most edge enhancement algorithms. In addition, the HS algorithm requires only a few lines of computer code, which makes it very simple to implement on any computer platform and enables a fast mean for enhancing edges. Performing an edge enhancement of our portal images and DRRs would improve the accuracy and speed of the rotation registration. Preliminary tests, illustrated in Fig. 5.1, reveal that during image registration, the full width half maximum (FWHM) of our cost function is reduced when we enhance the edges of a portal reference image and the corresponding portal test image, which contains both translational and rotational errors. A smaller FWHM is desirable when using a minimization algorithm because it will converge faster to the overall maximum correlation coefficient, thus making rotation registration faster and more accurate, since the peak of the cost-function will be sharper and easily detected.

We suggest an analysis of our method when using non-orthogonal portal images. Our method, in its present form is theoretically capable of functioning even with non-orthogonal portal images. For the simple example illustrated in Fig. 5.2 we have two non-orthogonal portal images. During registration, the algorithm should be capable of determining the rotation angle θ, which corresponds to the gantry angle used to acquire the oblique image, if we allow it to iterate up to that angle value. Once the gantry angle

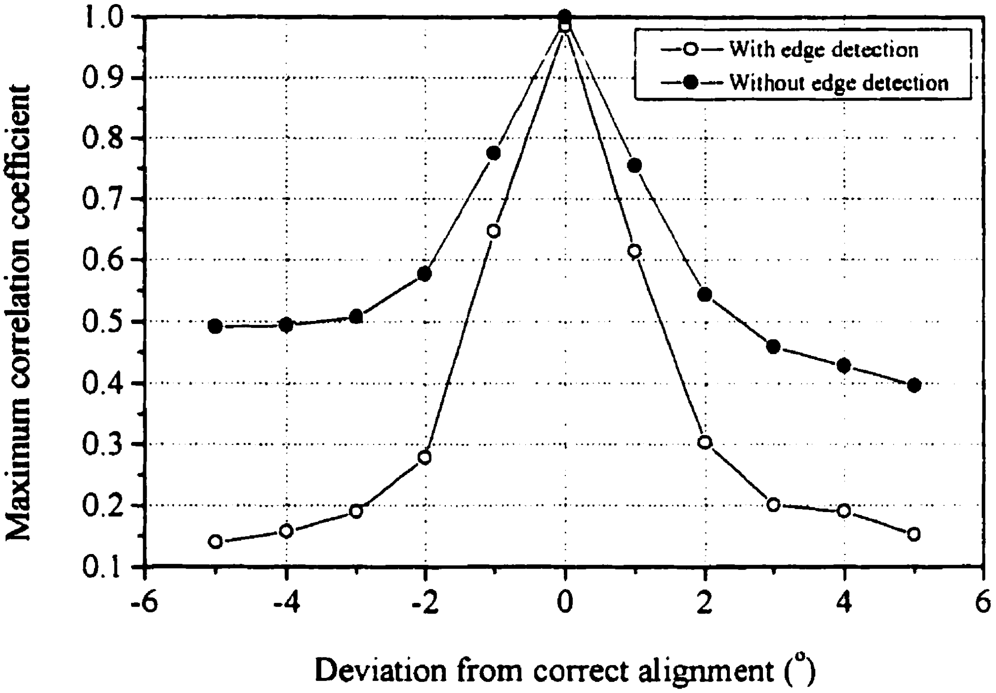

Figure 5.1: Maximum correlation coefficient as a function of rotational alignment deviations introduced in the test image using images with and without enhanced edges. We selected the histogram edge detection/enhancement algorithm for our purposes. The FWHM of the cost function is clearly wider when no edge enhancement is performed.

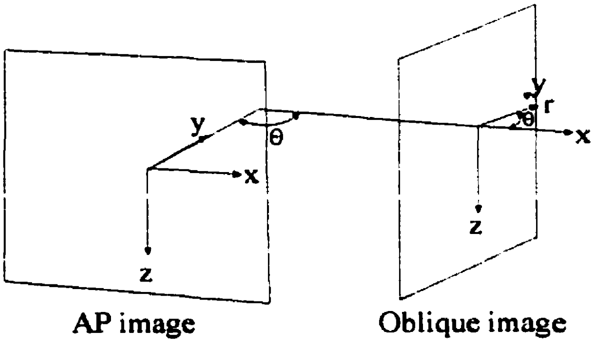

Figure 5.2: Graphical example of the implications of using non-orthogonal images.

used to acquire the oblique image is known, any translational positioning error detected within this image can be determined and decomposed into corresponding x, y and z positioning values using simple geometry. The Tz translational error is determined directly and the Tx and Ty decompositions of the vector $\boldsymbol{r}$ are

$$Tx = r\cos\theta \tag{5.1}$$

$$Ty = r\sin\theta \tag{5.2}$$

where Tx, Ty and Tz are the translational positioning errors along the x, y and z axes of a reference coordinate system.

An investigation of an non-orthogonal portal film approach should provide experimental results that test the accuracy of such an approach for determining translations, in-plane rotations and out-of-plane rotations. Because of the difficulty involved in obtained perfectly orthogonal portal films, a non-orthogonal film method would allow more flexibility during image acquisition.

Another approach to single film portal-to-DRR registration is to use the behavior of the cost-function as a tool for detecting changes in the magnification of the DRR. In an ideal situation, where the search image is identical to the reference image, the overall maximum correlation coefficient will be obtained when the magnification factors of both images are identical. Since the position of the detector is usually well known, differences in magnification can enable the user to determine translational errors along the plane perpendicular to the imaging plane by simply generating DRRs with varying source-to-axis distances until the overall maximum correlation value is found. However, this approach would require that the position of the portal detector from the source be known with great accuracy, that the DRRs be generated with high details and that the cost-function peak be very well defined. Once again, the HS edge detection/enhancement algorithm would prove to be ideal for such a task. Implementing a minimization algorithm with this technique would reduce the number of iterations involved and assure convergence of the cost function at the overall maximum correlation coefficient.

Finally although our technique was thoroughly tested for the head region only, it is as effective for other typical treatment regions. As a preliminary investigation, we registered a portal image of a pelvic region and matched it with a version of the same region that contained translations, in-plane rotations and both translations and in-plane rotations alignment errors. From the 20 matching tests performed, the algorithm was able to determine all the errors introduced in the test image. No deviations from the correct alignments were observed during registration. We suggest a thorough investigation of the feasibility of our method for registering images from various regions of the body and determining translations, in-plane rotations and out-of-plane rotation alignment errors.

5.3 REFERENCES

[1] D. H. Hristov and B. G. Fallone, "A grey-level image alignment algorithm for registration of portal images and digitally reconstructed radiographs," Med. Phys. 23, 75-84 (1996).

[2] K. Otto and B. G. Fallone, "Frame slippage verification in stereotactic radiosurgery," Int. J. Radiat. Oncol. Biol. Phys. 41, 199-205 (1998).

[3] A. Lujan, J. M. Balter, and R. K. en Haken, "Determination of rotations in three dimensions using two-dimensional portal image registration," Med. Phys. 25, 703-708 (1998).

[4] K. G. A. Gilhuijs, P. J. H. van de Ven, and M. van Herk, "Automatic three-dimensional inspection of patient setup in radiation therapy using portal images, simulator images, and computed tomography data," Med. Phys. 23, 389-399 (1996).

[5] M. J. Murphy, "An automatic six-degree-of-freedom image registration algorithm for image-guided frameless stereotaxic radiosurgery," Med. Phys. 24, 857-866 (1997).

[6] L. Lemieux, R. Jagoe, D. R. Fish, N. D. Kitchen, and D. G. T. Thomas, "A patient-to-computed tomography image registration method based on digitally reconstructed radiographs," Med. Phys. 21, 1749-1760 (1994).

[7] I. Rabinowitz, J. Broomberg, M. Goitein, K. McCarthy, and J. Leong, "Accuracy of radiation field alignment in clinical practice," Int. J. Radiat. Oncol. Biol. Phys. 11, 1857-1867 (1985).

[8] M. C. Schell, F. J. Bova, D. A. Larson and al., "Stereotactic Radiosurgery, Report of Task Group 42 Radiation Therapy Committee," AAPM report no. 54, 6-7 (1995).

[9] D. L. G. Hill and D. J. Hawkes, "Medical image registration using knowledge of adjacency of anatomical structures," Image Vision Comput. 12, 173-178 (1994).

[10] I. Crooks and B. G. Fallone, "A novel algorithm for the edge detection and edge enhancement of medical images," Med. Phys. 20, 993-998 (1993).

Bibliography

Note: The page number where the reference is cited is found in the brackets at the end of each entry.

3M diagnostic head phantom, 3M Corporation, St. Paul, Minnesota **(p. 33)**.

Advanced Visual Systems, Waltham, Massachusetts **(p.43)**.

J. M. Balter, C. A. Pelizzari, and G. T. Y. Chen, "Correlation of projection radiographs in radiation therapy using open curve segments and points," Med. Phys. 19, 329-335 (1992) **(p. 6, 8, 10)**.

G. Bergefors, "Hierarchical chamfer matching: a parametric edge matching algorithm," IEEE Transactions on Pattern Analysis and Machine Intelligence 10, 849-865 (1988) **(p. 6)**.

J. Bijhold, "Fast evaluation of patient set-up during radiotherapy by aligning features in portal and simulator images," Phys. Med. Biol. 36, 1665-1679 (1991) **(p. 5, 8)**.

R. N. Bracewell, "The Fourrier Transform and its Applications," (Montreal , 1978), 444 **(p. 23)**.

Clinac 18 linear accelerator, Varian Associates, Palo Alto, California **(p. 33)**.

C. Constantinou, J. C. Harrington, and A. DeWerd, "An electron density calibration phantom for CT based treatment planning computers," Med. Phys. 19, 325-327 (1992) **(p. 41)**.

I. Crooks and B. G. Fallone, "A novel algorithm for the edge detection and edge enhancement of medical images," Med. Phys. 20, 993-998 (1993) **(p. 10, 78)**.

E. I. Du Pont de Nemours & Co. Inc. Wilmington, Delaware, **(p. 34)**.

K. Eilersten, A. Skretting, and T. L. Tennvassas, "Methods for fully automated verification of patient set-up in external beam radiotherapy with polygon shaped fields," Phys. Med. Biol. 39, 993-1012 (1994) **(p. 5)**.

M. Garity, "Ray tracing irregular volume data. Proceedings of the 1990 San Diego Workshop on Volume Visualization," Computer Graphics 24, 35-40 (1990) **(p. 42)**.

K. G. A. Gilhuijs and M. van Herk, "Automatic on-line inspection of patient setup in radiation therapy using digital portal images," Med. Phys. 20, 667-677 (1993) **(p. 6)**.

K. G. A. Gilhuijs, P. J. H. van der Ven, and M. van Herk, "Automatic three-dimensional inspection of patient setup in radiation therapy using portal images, simulator images, and computed tomography data," Med. Phys. 23, 389-399 (1996) **(p. 9, 75)**.

M. Goitein, M. Abrams, D. Rowell, H. Pollari, and J. Wiles, "Multi-dimensional treatment planning: beam's eye view, back projection, and projection through sections," Int. J. Radiat. Oncol. Biol. Phys. 9, 789-797 (1983) **(p. 35)**.

J. Hanley, G. S. Mageras, J. Sun, and G. J. Kutcher, "The effects of out-of-plane rotations on two-dimensional portal image registration in conformal radiotherapy of the prostate," Int. J. Radiat. Oncol. Biol. Phys. 33, 1331-1343 (1995) **(p. 8)**.

H. F. Hare, J. Hale, and E. P. Pendergrass, "Physical and clinical aspects of supervoltage rotational therapy," Radiology 57, 157 (1951) **(p. 2)**.

D. L. G. Hill and D. J. Hawkes, "Medical image registration using knowledge of adjacency of anatomical structures," Image Vision Comput. 12, 173-178 (1994) **(p. 77)**.

HP 9000 P 735/125 Workstation, Hewlett-Packard Company, Palo Alto, California **(p.43)**.

D. H. Hristov and B. G. Fallone, "A grey-level image alignment algorithm for registration of portal images and digitally reconstructed radiographs," Med. Phys. 23, 75-84 (1996) **(p. 7, 11, 21, 22, 23, 28, 29, 32, 75, 77)**.

H. E. Johns and J. R. Cunningham, "The Physics of Radiology," (Charles C. Thomas, Springfield , 1983), 796 **(p. 37)**.

S. M. Jones and A. L. Boyer, "Investigation of an FFT-based correlation technique for verification of radiation setup," Med. Phys. 18, 1116-1125 (1991) **(p. 7, 20)**.

Leksell Stereotactic Frame, Elekta Instrument AB, Stockholm, Sweden, **(p. 33)**.

L. Lemieux, R. Jagoe, D. R. Fish, N. D. Kitchen, and D. G. T. Thomas, "A patient-to-computed tomography image registration method based on digitally reconstructed radiographs," Med. Phys. 21, 1749-1760 (1994) **(p. 8, 75, 77)**.

K. Leszczynski, S. Loose, and P. Dunscombe, "Segmented chamfer matching for the registration of field borders in radiotherapy images," Phys. Med. Biol. 40, 83-94 (1995) **(p. 5)**.

A. Lujan, J. M. Balter, and R. K. en Haken, "Determination of rotations in three dimensions using two-dimensional portal image registration," Med. Phys. 25, 703-708 (1998) **(p. 10, 75)**.

E. C. McCullough and T. W. Holmes, "Acceptance testing computerized radiation treatment planning systems: Direct utilization of CT scan data," Med. Phys. 12, 237-242 (1985) **(p. 41)**.

J. Moseley and P. Munro, "A semiautomatic method for registration of portal images," Med. Phys. 21, 551-558 (1994) **(p. 7, 9)**.

M. J. Murphy, "An automatic six-degree-of-freedom image registration algorithm for image-guided frameless stereotaxic radiosurgery," Med. Phys. 24, 857-866 (1997) **(p. 9, 75)**.

E. Orfali, "Verification of a 3D external photon beam treatment planning system," McGill University, M.Sc. dissertation (1996) **(p. 41)**.

K. Otto, "3-Dimensional Anatomy-Based Verification in Stereotactic Radiosurgery," McGill University, M.Sc. dissertation (1997) **(p. 10, 11)**.

K. Otto and B. G. Fallone, "Frame slippage verification in stereotactic radiosurgery," Int. J. Radiat. Oncol. Biol. Phys. 41, 199-205 (1998) **(p. 10, 11, 32, 75)**.

R. P. Parker, P. A. Hobday, and K. J. Cassell, "The direct use of CT numbers in radiotherapy dosage calculations for inhomogeneous media," Phys. Med. Biol. 24, 802-809 (1979) **(p. 40)**.

E. B. Podgorsak, B. Pike, A. Olivier, M. Pla, and L. Souhami, "Radiosurgery with high energy photon beams: A comparison among techniques," Int. J. Radiat. Oncol. Biol. Phys. 16, 857-865 (1989) **(p. 4)**.

W. Pratt, "Digital Image Processing," (New York , 1978) **(p. 21)**.

I. Rabinowitz, J. Broomberg, M. Goitein, K. McCarthy, and J. Leong, "Accuracy of radiation field alignment in clinical practice," Int. J. Radiat. Oncol. Biol. Phys. 11, 1857-1867 (1985) **(p. 4, 76)**.

R. J. Schalkoff, "Digital Image Processing and Computer Vision," (Wiley, New York, 1989), 279-284 **(p. 18, 19)**.

M. C. Schell, F. J. Bova, D. A. Larson, D. D. Leavitt, W. R. Lutz, E. P. Podgorsak, and A. Wu, "Stereotactic Radiosurgery, Report of Task Group 42 Radiation Therapy Committee," AAPM report no. 54, 6-7 (1995) **(p. 4, 76)**.

G. W. Sherouse, "Coordinate transformations as a primary representation of radiotherapy beam geometry," Med. Phys. 19, 175-179 (1992) **(p. 45)**.

R. Siddon, "Solution to treatment planning problems using coordinate transformations," Med. Phys. 8, 766-774 (1981) **(p. 33)**.

J. Wong, E. D. Slessinger, R. E. Hermes, C. J. Offutt, T. Roy, and M. W. Vannier, "Portal dose images I: Quantitative treatment plan verification," Int. J. Radiat. Oncol. Biol. Phys. 18, 389-399 (1990) **(p. 8)**.

X-Omatic radiation therapy cassette, Eastman Kodak Co., Rochester, New York **(p. 33)**.

List of Figures

Figure 3.4: In order to compare the data from two different coordinate systems, a common coordinate system must be determined. Using a volume transformation matrix (VTM), it is possible to transform our CT-data from the CT-coordinate system to the world coordinate system.

Figure 3.5: 2-D correlation matrix resulting from correlating the AP portal search mask with the AP DRR search window. The location where the search mask best matches the search window is represented by the location of the maximum correlation coefficient. The intensity of each pixel represents the correlation value at that point.

Figure 3.6: 2-D correlation matrix resulting from correlating the LAT portal search mask with the LAT DRR search window. The location where the search mask best matches the search window is represented by the location of the maximum correlation coefficient. The intensity of each pixel represents the correlation value at that point.

Figure 3.7: 3-D representation of the correlation matrix resulting from correlating the AP portal search mask with the AP DRR search window. Although several local minima and maxima are typically observed in the correlation matrix, the overall maximum correlation value clearly stands out and enables us it's position in the 2-D matrix.

Figure 3.8: 3-D representation of the correlation matrix resulting from correlating the LAT portal search mask with the LAT DRR search window. Although several local minima and maxima are typically observed in the correlation matrix, the overall maximum correlation value clearly stands out and enables us it's position in the 2-D matrix.

Figure 3.9: Schematic illustration of the orthogonal imaging acquisition set-up. It becomes evident that a displacement along Ty will affect the projected magnification of the Tx displacement and vice versa.

Figure 4.1: AP DRR illustrating the four search masks selected for DRR-to-DRR image registration.

Figure 4.2: LAT DRR illustrating the four search masks selected for DRR-to-DRR image registration.

Figure 4.3: Results of DRR-to-DRR translation tests. Plotted are the mean and standard deviations between the actual positions and the ones given by the registration algorithm during registration along the *Tx*, *Ty* and *Tz* translation components. Each point is the result of the registration of a zero displacement DRR and 1331 randomly generated DRRs not exceeding ± 15 mm from the actual position.

Figure 4.4: Results of DRR-to-DRR translation and rotation registration tests. Plotted are the mean and standard deviations between the actual alignment and the one given by the registration algorithm during registration along the *Tx*, *Ty* and *Tz* translation axes and *AP*, *SI* and *RL* rotation axes. Each point is the result of the registration of a zero displacement DRR and 343 randomly generated DRRs not exceeding ± 15 mm for translation and ± 4.5° for rotations from the actual alignment.

Figure 4.5: Results of DRR-to-DRR translation and rotation registration tests. Plotted are the mean differences and standard deviations between the correct rotation alignment and the rotation alignment given by the registration algorithm using features 2, 5 and 6 along the *AP*, *SI* and *RL* rotation axes.

Figure 4.6: Maximum correlation coefficient as a function of translations along the X and Z stereotactic axes for feature 2 (AP view).

Figure 4.7: Maximum correlation coefficient as a function of translations along the Y and Z axes for feature 6 (LAT view).

Figure 4.8: Maximum correlation coefficient as a function of in-plane displacements along the X-axis measured at different displacements along the Y-axis (perpendicular to the imaging plane) for feature 2 in the AP view.

Figure 4.9: Maximum correlation coefficient as a function of in-plane displacements along the Z-axis measured at different displacements along the Y-axis (perpendicular to the imaging plane) for feature 2 in the AP view.

Figure 4.10: Maximum correlation coefficient as a function of in-plane displacements along the Y-axis measured at different displacements along the X-axis (perpendicular to the imaging plane) for feature 6 in the LAT view.

Figure 4.11: Maximum correlation coefficient as a function of in-plane displacements along the Z-axis measured at different displacements along the X-axis (perpendicular to the imaging plane) for feature 6 in the LAT view.

Figure 4.12: Results of portal-to-DRR translation registration tests. Plotted are the maximum, mean and median alignment errors between the correct alignment and the alignment given by the registration algorithm with 3 pairs of orthogonal portal images and 375 DRR pairs simulated at random *Tx*, *Ty* and *Tz* isocentre positions within ± 15 mm of the correct position. The error bars represent the standard deviation.

Figure 4.13: Results of portal-to-DRR translation and rotation registration tests. Plotted are the maximum, mean and median alignment errors between the correct alignment and the alignment given by the registration algorithm with 3 pairs of orthogonal portal images and 15 DRR pairs simulated at random *Tx*, *Ty* and *Tz* within ± 15 mm of the correct position. The error bars represent the standard deviation.

Figure 5.1: Maximum correlation coefficient as a function of rotational alignment deviations introduced in the test image using images with and without enhanced edges. We selected the histogram edge detection/enhancement algorithm for our purposes. The FWHM of the cost function is clearly wider when no edge enhancement is performed.

Figure 5.2: Graphical example of the implications of using non-orthogonal images.